Direct measurement of dark matter halo ellipticity from two-dimensional lensing shear maps of 25 massive clusters *

Masamune Oguri,[1,2]† Masahiro Takada,[3] Nobuhiro Okabe[4,5] and Graham P. Smith[6]

[1]*Division of Theoretical Astronomy, National Astronomical Observatory of Japan, 2-21-1 Osawa, Mitaka, Tokyo 181-8588, Japan.*
[2]*Kavli Institute for Particle Astrophysics and Cosmology, Stanford University, 2575 Sand Hill Road, Menlo Park, CA 94025, USA.*
[3]*Institute for the Physics and Mathematics of the Universe (IPMU), The University of Tokyo, Chiba 277-8582, Japan.*
[4]*Institute of Astronomy and Astrophysics, Academica Sinica, PO Box 23-141, Taipei 106, Taiwan.*
[5]*Astronomical institute, Tohoku University, Aramaki, Aoba-ku, Sendai, 980-8578, Japan.*
[6]*School of Physics and Astronomy, University of Birmingham, Edgbaston, Birmingham B15 2TT.*

27 April 2010

ABSTRACT

We present new measurements of dark matter distributions in 25 X-ray luminous clusters by making a full use of the two-dimensional (2D) weak lensing signals obtained from high-quality Subaru/Suprime-Cam imaging data. Our approach to directly compare the measured lensing shear pattern with elliptical model predictions allows us to extract new information on the mass distributions of individual clusters, such as the halo ellipticity and mass centroid. We find that these parameters on the cluster shape are little degenerate with cluster mass and concentration parameters. By combining the 2D fitting results for a subsample of 18 clusters, the elliptical shape of dark matter haloes is detected at 7σ significance level. The mean ellipticity is found to be $\langle e \rangle = \langle 1 - b/a \rangle = 0.46 \pm 0.04 \, (1\sigma)$, which is in excellent agreement with a theoretical prediction based on the standard collisionless cold dark matter model. The mass centroid can be constrained with a typical accuracy of ~ 20 arcseconds ($\sim 50h^{-1}$ kpc) in radius for each cluster. The mass centroid position fairly well matches the position of the brightest cluster galaxy, with some clusters showing significant offsets. Thus the 2D shear fitting method enables to assess one of the most important systematic errors inherent in the stacked cluster weak lensing technique, the mass centroid uncertainty. In addition, the shape of the dark mass distribution is found to be only weakly correlated with that of the member galaxy distribution or the brightest cluster galaxy. We carefully examine possible sources of systematic errors in our measurements including the effect of substructures, the cosmic shear contamination, fitting regions, and the dilution effect, and find none of them to be significant. Our results demonstrate the power of high-quality imaging data for exploring the detailed spatial distribution of dark matter, which should improve the ability of future surveys to conduct cluster cosmology experiments.

Key words: dark matter — galaxies: clusters: general — gravitational lensing

1 INTRODUCTION

The internal structure of clusters predicted by N-body simulations of the collisionless Cold Dark Matter (CDM) universe exhibits several important features, including the universal radial density profile with progressively shallower slopes toward the centre (e.g., Navarro et al. 1996, 1997)

and the highly non-spherical structure fitted well by a triaxial density profile (e.g., Jing & Suto 2002). These features are closely related to the cold and collisionless nature of hypothetical dark matter particles (e.g., Ostriker & Steinhardt 2003), which suggests that detailed observational tests of cluster density profiles may provide a clue to the nature of dark mater. In addition, an accurate determination of the mass distribution of individual clusters is also important in calibrating observable-mass relations which are necessary for constraining cosmological parameters from cluster abundance (e.g., Bahcall & Cen 1993; Eke et al. 1996;

Kitayama & Suto 1997; Henry 2000; Borgani et al. 2001; Bahcall & & Bode 2003; Dahle 2006; Mantz et al. 2008; Henry et al. 2009; Vikhlinin et al. 2009; Rozo et al. 2010).

Gravitational lensing is one of the most powerful methods to constrain the cluster mass distribution. This is because gravitational lensing probes the matter distribution directly, regardless of whether it is luminous or dark. This is in marked contrast with other probes such as X-ray and Sunyaev-Zel'dovich effect for which assumptions on gas state and other pressure components are crucial in extracting the mass distribution. In particular the cluster mass distribution has extensively been studied using weak lensing technique which makes use of small distortions of background galaxies produced by a foreground cluster (see Bartelmann & Schneider 2001, for a review). Indeed the weak lens technique has been quite successful in constraining dark matter distributions in clusters independently of the distribution of the hot gas component (Kneib et al. 2003; Clowe et al. 2006; Jee et al. 2007; Mahdavi et al. 2007, 2008; Okabe & Umetsu 2008; Bradač et al. 2008).

While the weak lensing technique allows the non-parametric reconstruction of the mass map (Kaiser & Squires 1993), azimuthally-averaged one-dimensional (1D) tangential shear profiles have been used in most of quantitative studies so far (e.g., Bardeau et al. 2007; Broadhurst et al. 2008; Hamana et al. 2009; Oguri et al. 2009; Okabe et al. 2010). The main reason for this is that the 1D profile fitting provides an easy and efficient way to extract several important cluster properties, such as mass, concentration, and radial density profiles of clusters. However, the highly non-spherical nature of CDM haloes predicted by N-body simulations indicates that the full two-dimensional (2D) study of weak lensing data is crucial for further tests of the cluster mass distribution. Moreover, an important disadvantage of the 1D profile fitting is that we have to assume the centre of the cluster a priori. It has often been assumed that the mass centroid coincides with the location of the brightest cluster galaxy (BCG), despite the fact that offsets of BCGs from the mass centroids appear to be common (e.g., Katayama et al. 2003; Lin & Mohr 2004; Koester et al. 2007; Ho et al. 2009; Sanderson et al. 2009). The 2D weak lensing studies with non-spherical mass models have been attempted, but only for a handful of lensing clusters (e.g., Cypriano et al. 2004; Deb et al. 2010). Fitting of weak lensing data by taking fully into account a 3D (triaxial) cluster shape and the projection along arbitrary line-of-sight has been performed by Oguri et al. (2005), and later by Corless et al. (2009), but their interests lied in the determination of masses and concentration parameters rather than the shape of the projected mass distribution. Given the strong selection bias of the apparent 2D cluster ellipticity for lensing clusters (Oguri & Blandford 2009), more systematic 2D weak lensing studies of massive clusters should be conducted using well-defined statistical cluster samples.

Cluster mass distributions have also been studied in details using stacked weak lensing data (Sheldon et al. 2007a,b; Johnston et al. 2007; Mandelbaum et al. 2006b, 2008). Although the stacked weak lensing technique is quite successful in extracting average properties of clusters, its main disadvantage comes from the centroid problem (e.g., Johnston et al. 2007; Mandelbaum et al. 2010); in stacking

clusters one has to assume a priori the mass centroid for each cluster. The misidentification of the mass centroid results in the suppression of weak lensing signals, particularly near the cluster centre. Recently, Evans & Bridle (2009) measured the ellipticity of isolated clusters with stacked weak lensing technique to obtain the average cluster ellipticity of $e \sim 0.5$. However, their result is built on the assumption that the cluster mass distributions is aligned with the spatial distribution of member galaxies, and also on the assumption about the cluster centre, which makes the interpretation somewhat difficult.

In this paper, we present a systematic 2D study of weak lensing maps. We analyse 25 clusters at $0.15 < z < 0.3$ presented by Okabe et al. (2010), who examined azimuthally-averaged 1D tangential profiles to study the radial mass profiles of the clusters. The cluster sample is essentially X-ray flux-limited statistical sample from the Local Cluster Substructure Survey (LoCuSS; G. Smith et al., in preparation). In this paper we extend the lensing analysis of Okabe et al. (2010) and perform a full 2D fitting of the shear fields with particular emphasis on the projected 2D ellipticities of the clusters. All the weak lensing data are based on optical images taken with Subaru/Suprime-cam (Miyazaki et al. 2002) which is known to be the current best ground facility for weak lensing studies because of its exquisite image quality and wide field-of-view (e.g., Kasliwal et al. 2008). In our analysis we leave the centre of the mass profile as a free parameter and fit it simultaneously in order to see how the 2D analysis of shear maps constrains the cluster mass centroid which has often been assumed to coincide with the location of the BCG. Our approach to fit individual clusters with the centroid and orientation of the cluster as free parameters not only overcomes the problems inherent to stacked weak lensing technique but also allows us to even test the assumptions on the centroid and orientation from weak lensing data alone.

The structure of this paper is as follows. We describe our fitting procedure in §2, and present results in §3. In §4 we discuss possible systematic effects, and in §5 we draw our conclusions. Throughout the paper we assume a flat universe with the matter density $\Omega_M = 1 - \Omega_\Lambda = 0.274$, the dimensionless Hubble constant $h = 0.704$, the baryon density $\Omega_b h^2 = 0.02267$, the spectral index $n_s = 0.96$, and the normalisation of the matter power spectrum $\sigma_8 = 0.812$ (Komatsu et al. 2009).

2   DATA ANALYSIS

2.1   Cluster sample

In this paper, we study the same cluster sample as in Okabe et al. (2010). The sample comprises 30 massive clusters observed with Subaru/Suprime-cam, and represents an unbiased subsample of the LoCuSS clusters, an all-sky sample of ~ 100 X-ray luminous ($L_X \gtrsim 2 \times 10^{44} \mathrm{erg\,s^{-1}}$) galaxy clusters located at $0.15 < z < 0.3$ selected from the ROSAT All Sky Survey catalogues (Ebeling et al. 1998, 2000; Böhringer et al. 2004). Since X-ray properties of clusters are not very much affected by the degree of the elongation along the line-of-sight (e.g., Gavazzi 2005), the orientation bias, which is important for lensing-selected clusters

(Hennawi et al. 2007; Oguri & Blandford 2009), is expected to be insignificant for our sample.

The properties of the clusters and the basic parameters of the Subaru/Suprime-cam observations are summarised in Table 1 of Okabe et al. (2010). All the 30 clusters were observed with sub-arcsecond seeing conditions. Among these 25 clusters have two-filter images (mostly V- and i-bands, with typical exposure time of $\sim 20 - 40$ minutes for each filter), whereas for the other 5 clusters only one-filter images are available. The colour information is very important to minimise the dilution effect by cluster member galaxies (see also Broadhurst et al. 2005). In addition, the colour information allows to define a sample of member galaxies from galaxies around the red sequence locus in the colour-magnitude diagram, and to compare the member galaxy distribution with the mass distribution constrained from lensing observables. Thus, in this paper we restrict our analysis to the 25 clusters with colour information. As a fiducial background galaxy population, we adopt "red+blue" galaxy sample defined as faint galaxies with colours redder or bluer than the red-sequence by properly chosen offsets. As shown in Okabe et al. (2010), the dilution effect by member galaxies appears to be quite small for this source galaxy sample. The effective source redshift, which is defined such that the lensing depth D_{ls}/D_s (D_{ls} and D_s being the angular diameter distances from the lens to the source and from the observer to the source, respectively) at that redshift becomes equal to the mean lensing depth averaged over the background galaxy population, is estimated by matching magnitudes and colours of the background galaxies to COSMOS photometric redshift catalogue of Ilbert et al. (2009). See Okabe et al. (2010) for more detailed descriptions.

2.2 Weak lensing data

Weak lensing distortion measurements enable a direct reconstruction of the projected 2D mass distribution (Kaiser & Squires 1993). However, the non-local nature of the mass reconstruction indicates that reconstructed mass densities between different pixels in the mass map are highly correlated. Thus one has to take account of the full covariance matrix of the mass map in order to extract proper information from the mass map, as done in Oguri et al. (2005) and Umetsu & Broadhurst (2008). In this paper, we avoid this complication by working directly on the 2D distortion maps.

We use the weak lensing distortion measurements presented by Okabe et al. (2010). For each cluster field, the reduced distortion, $g_\alpha = \gamma_\alpha/(1 - \kappa)$, was estimated from the shape of each source galaxy by analysing the Subaru/Suprime-cam images based on the algorithm described in Kaiser et al. (1995). Throughout this paper we employ the convention that the Greek subscripts denote the two components of distortion, e.g., $\alpha = 1$ or 2. The lensing distortion is not measurable from individual galaxy image due to the dominant intrinsic shape noise. Instead the signal is measurable in a statistical sense, i.e., by averaging the galaxy shapes over a sufficient number of galaxies. Given the deep Subaru images and the distortion strength in a cluster region, the angular resolution of weak lensing distortion is an arcminute scale. In order to conduct the full two-dimensional analysis of distortion fields, we employ the pixelised data of

background galaxy shapes. Specifically, the reduced shear in the l-th pixel (its angular position $\boldsymbol{\theta}_l$) is estimated as

$$\langle g_\alpha \rangle (\boldsymbol{\theta}_l) = \left[\sum_{\boldsymbol{\theta}_i \in \boldsymbol{\theta}_l} w_i g_\alpha(\boldsymbol{\theta}_i) \right] \left[\sum_{\boldsymbol{\theta}_i \in \boldsymbol{\theta}_l} w_i \right]^{-1}, \quad (1)$$

where $\boldsymbol{\theta}_i$ denotes the angular position of the i-th source galaxy and the summation runs over source galaxies contained within the l-th pixel. Following Okabe et al. (2010) we use the weighting of each galaxy shape such that a galaxy whose shape is more reliably measured is assigned a larger weight. The weight w_i for the i-th galaxy is given by

$$w_i = \frac{1}{a^2 + \sigma_{g(i)}^2}, \quad (2)$$

with $a = 0.4$ and $\sigma_{g(i)}$ being the uncertainty of shape measurement for each galaxy (see Okabe et al. 2010). As stated above, the dominant source of distortion measurement error is the intrinsic galaxy shape. The shape noise in each pixel is estimated as

$$\sigma_g^2(\boldsymbol{\theta}_l) = \frac{1}{2} \left[\sum_{\boldsymbol{\theta}_i \in \boldsymbol{\theta}_l} w_i^2 \sigma_{g(i)}^2 \right] \left[\sum_{\boldsymbol{\theta}_i \in \boldsymbol{\theta}_l} w_i \right]^{-2}. \quad (3)$$

For all the clusters we adopt a grid size of $1' \times 1'$ (we tried smaller grid sizes and found that the results are almost unchanged; see also Appendix A). We do not use four innermost grids ($2' \times 2'$ box) for the fitting, because source galaxies are obscured by dense distribution of cluster member galaxies especially in the central region, and also because our assumption of single source redshift may become inaccurate near the cluster centre due to the fewer sampling of source galaxies. Moreover, the weak lensing approximation breaks down near the cluster centre. Although the field-of-view of Subaru/Suprime-cam is $34' \times 27'$, we conduct our fitting only in a $20' \times 20'$ region ($20'$ corresponds to physical transverse sizes of $2.2h^{-1}$ Mpc for $z = 0.15$ and $3.8h^{-1}$ Mpc for $z = 0.3$, respectively) centred at the BCG, which roughly corresponds to virial radii of clusters in our sample, in order to reduce the projection effect, i.e. the effect of different structures along the same line of sight, which is more prominent in the boundary region where the cluster lensing signal is very weak. However, it should be noted that this restriction of fitting region little affects the final results, as we will discuss later in more detail. Thus the total number of girds used for the fitting is $N_{\rm pixel} = 396$. An example of our weak lensing shear map is given in the left panel of Figure 1.

For the range of angular scales we use for the fitting, the measured distortion field is nearly the shear field, $g_\alpha \simeq \gamma_\alpha$, which we will simply assume in the following analysis.

2.3 Cluster mass model

We assume that the cluster mass distribution can be described by a single halo component with its radial profile being so-called NFW density profile (Navarro et al. 1996, 1997). The spherical NFW model is fully specified by two parameters, the halo concentration and mass parameters. Although the density profile was obtained from N-body simulation by spherically averaging the halo mass distribution,
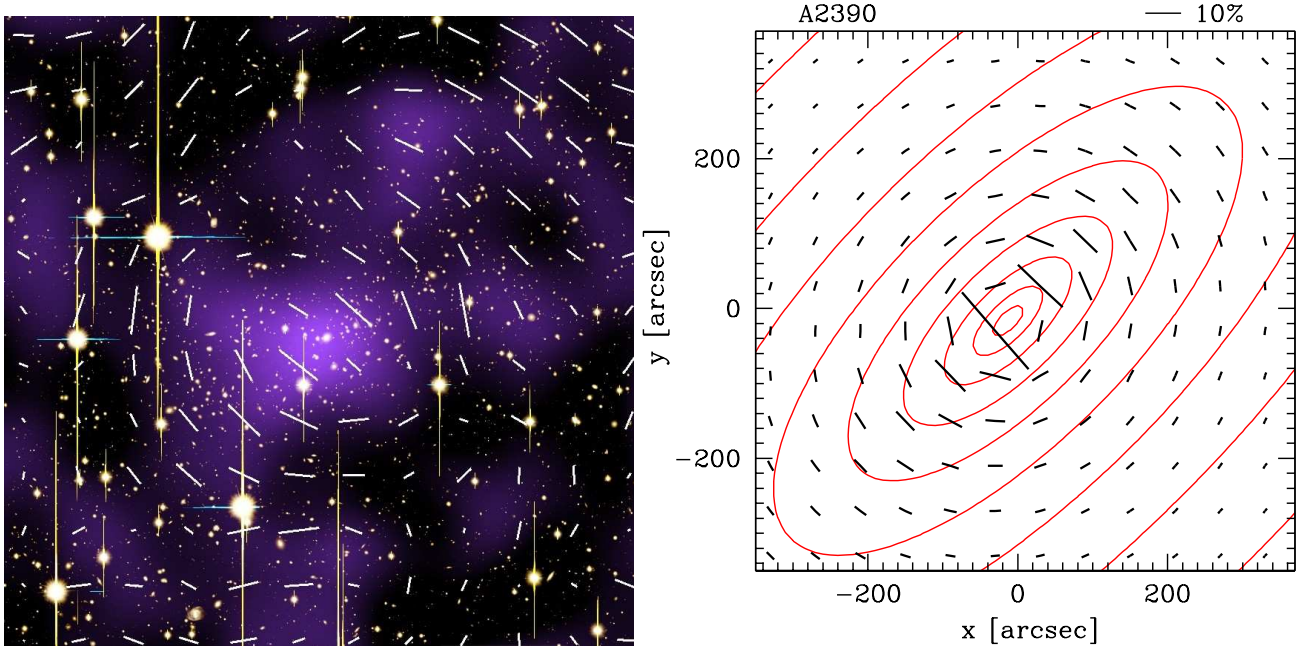
Figure 1. *Left panel:* An example of our weak lensing measurement for A2390. The size of Each panel is $12' \times 12'$. The stick in each $1' \times' 1$ pixel shows the distortion field estimated from background galaxy images contained within the pixel, where a background galaxy image is deformed along the stick direction, and the length is proportional to the shear amplitude. The shear field in this panel is smoothed with a Gaussian with the full width at half maximum of $\simeq 1.6'$ for illustrative purpose. Overplotted is the surface mass density map reconstructed from the weak lensing shear measurement (see Okabe et al. 2010). North is up and East is left. *Right panel:* The shear field predicted by our best-fit elliptical NFW model (see also Figure 2 and Table 1), while the contours are the isodensity map. The best-fit ellipticity of the projected mass density is $e \equiv 1 - b/a = 0.598$.

we can construct an elliptical lens model simply by introducing an ellipticity in the isodensity contour. Specifically, we adopt the following mass model in our analysis:

$$\kappa(x, y) = \kappa_{\mathrm{sph}}(\zeta), \tag{4}$$

$$\zeta^2 = \frac{x'^2}{1 - e} + (1 - e)y'^2, \tag{5}$$

$$x' = x \cos \theta_e + y \sin \theta_e, \tag{6}$$

$$y' = -x \sin \theta_e + y \cos \theta_e, \tag{7}$$

where $\kappa_{\mathrm{sph}}(r)$ is the radial convergence profile for the spherical NFW profile (e.g., Bartelmann 1996). Here the coordinate origin is taken as the halo centre (x_c, y_c). The halo ellipticity e is related with the major (a) and minor (b) axis lengths of the isodensity contour as $e = 1 - b/a$. Throughout the paper we adopt the coordinate system with the x- and y-axes being aligned with West and North respectively. With this coordinate system the position angle θ_e is measured East of North. The lensing shear is computed by solving the two-dimensional Poisson equation whose source term is given by the convergence $\kappa(x, y)$, as described in Schramm (1990). We note that this elliptical model includes a triaxial halo model which better describes haloes in N-body simulations than the spherical model (Jing & Suto 2002; Kasun & Evrard 2005; Allgood et al. 2006), because the convergence map of a triaxial halo has elliptical isodensity contours when projected along arbitrary directions (Oguri et al. 2003; Oguri & Keeton 2004).

In summary, the elliptical NFW model is specified by 6 model parameters:

$$\boldsymbol{p} \equiv \{M_{\mathrm{vir}}, c_{\mathrm{vir}}, e, \theta_e, x_c, y_c\}. \tag{8}$$

Unless otherwise specified, we adopt the virial overdensity $\Delta_{\mathrm{vir}} \simeq 110$ (with respect to the critical density of the universe) computed using the spherical collapse model to define the mass M_{vir} and the concentration parameter c_{vir}.

2.4   2D weak lensing fitting

The two-dimensional pixelised distortion field described in § 2.2 can be compared with the two-dimensional mass model in § 2.3 in order to constrain properties of halo mass distribution including the halo ellipticity. In this paper we employ the χ^2 fitting given as

$$
\begin{aligned}
\chi^2 &= \sum_{\alpha, \beta=1}^{2} \sum_{k,l=1}^{N_{\mathrm{pixel}}} [g_\alpha(\boldsymbol{\theta}_k) - g_\alpha^{\mathrm{m}}(\boldsymbol{\theta}_k; \boldsymbol{p})] \left[\boldsymbol{C}^{-1}\right]_{\alpha\beta, kl} \\
&\quad \times [g_\beta(\boldsymbol{\theta}_l) - g_\beta^{\mathrm{m}}(\boldsymbol{\theta}_l; \boldsymbol{p})],
\end{aligned} \tag{9}
$$

where the indices α and β run over the two components of distortion $(\alpha, \beta = 1, 2)$ and the indices k and l denote the pixel position $(k, l = 1, \ldots, N_{\mathrm{pixel}})$. The matrix $\boldsymbol{C}$ denotes the error covariance matrix and $\boldsymbol{C}^{-1}$ is the inverse matrix (see below).The best-fit model parameters are found by minimizing the χ^2 value given the distortion data.

For the covariance matrix we include two contributions: the intrinsic ellipticity noise, which is the primary source, and the cosmic shear contamination arising from large-scale structures at different redshifts, but along the same line of sight. The covariance matrix is expressed as

Table 1. Results of weak lensing analysis for 25 clusters, obtained by fitting the 2D shear maps with predictions of the elliptical NFW model. Note that the degree of freedom of the χ^2 fitting is 786. The coordinate origin in the fitting is taken as the BCG position for each cluster. The position angle θ_e is defined East of North. Each error indicates the 1σ error marginalised over other parameter uncertainties.

Name	z	χ^2	$x_{\rm c}$ (arcsec)	$y_{\rm c}$ (arcsec)	$M_{\rm vir}$ $(10^{14}h^{-1}M_\odot)$	$c_{\rm vir}$	e	θ_e (deg)
A68	0.2546	719.1	$44.8^{+12.2}_{-13.2}$	$23.7^{+16.9}_{-19.6}$	$7.83^{+6.84}_{-3.95}$	$3.10^{+3.71}_{-2.04}$	$0.552^{+0.174}_{-0.243}$	$-3.3^{+9.9}_{-38.1}$
A115[a]	0.1971	725.0	$-78.5^{+49.9}_{-11.8}$	$134.1^{+41.9}_{-148.8}$	$15.76^{+13.56}_{-3.50}$	$0.94^{+1.10}_{-0.30}$	$0.609^{+0.125}_{-0.212}$	$12.3^{+13.6}_{-2.7}$
A209	0.2069	844.3	$29.6^{+15.9}_{-8.7}$	$10.4^{+22.4}_{-16.9}$	$14.94^{+7.54}_{-4.46}$	$2.38^{+1.07}_{-0.79}$	$0.428^{+0.082}_{-0.188}$	$16.3^{+10.3}_{-17.8}$
RXJ0142	0.2803	827.5	$2.1^{+24.7}_{-2.9}$	$-7.1^{+15.7}_{-5.4}$	$4.68^{+1.68}_{-1.53}$	$5.87^{+6.10}_{-2.37}$	$0.799^{+0.030}_{-0.259}$	$-53.6^{+3.2}_{-6.9}$
A267	0.2300	749.0	$-0.0^{+7.7}_{-8.6}$	$5.8^{+16.2}_{-12.0}$	$3.27^{+0.66}_{-0.90}$	$10.04^{+11.74}_{-2.44}$	$0.769^{+0.069}_{-0.094}$	$26.5^{+3.2}_{-5.5}$
A291	0.1960	807.3	$11.2^{+9.9}_{-22.6}$	$-48.0^{+33.4}_{-19.6}$	$5.60^{+2.86}_{-1.52}$	$2.94^{+1.75}_{-1.09}$	$0.771^{+0.062}_{-0.094}$	$33.9^{+3.8}_{-4.6}$
A383	0.1883	840.2	$-4.2^{+2.6}_{-3.2}$	$-3.3^{+0.9}_{-16.2}$	$2.01^{+0.28}_{-0.15}$	$34.14^{+5.55}_{-8.92}$	$0.814^{+0.067}_{-0.072}$	$-5.3^{+1.6}_{-1.6}$
A521	0.2475	818.3	$0.3^{+19.2}_{-62.3}$	$-54.6^{+31.9}_{-42.8}$	$13.63^{+7.76}_{-5.35}$	$1.29^{+0.70}_{-0.61}$	$0.176^{+0.206}_{-0.175}$	$-7.4^{+91.3}_{-80.1}$
A586	0.1710	838.7	$-9.0^{+16.5}_{-18.8}$	$-10.2^{+14.6}_{-9.7}$	$6.16^{+3.49}_{-2.52}$	$8.67^{+9.37}_{-3.72}$	$0.426^{+0.212}_{-0.248}$	$-87.7^{+25.8}_{-15.2}$
ZwCl0740	0.1114	825.7	$-46.4^{+21.9}_{-14.4}$	$44.9^{+26.0}_{-28.7}$	$18.65^{+20.79}_{-6.74}$	$1.57^{+0.82}_{-0.62}$	$0.553^{+0.117}_{-0.147}$	$19.3^{+7.0}_{-10.0}$
ZwCl0823	0.2248	867.4	$45.9^{+25.8}_{-14.5}$	$26.5^{+10.6}_{-10.3}$	$9.78^{+7.25}_{-3.71}$	$2.75^{+1.91}_{-1.22}$	$0.144^{+0.258}_{-0.144}$	$-47.3^{+137.2}_{-42.4}$
A611	0.2880	779.7	$-17.5^{+22.1}_{-10.6}$	$25.9^{+13.9}_{-24.7}$	$11.08^{+7.91}_{-2.70}$	$1.95^{+0.94}_{-0.97}$	$0.517^{+0.127}_{-0.110}$	$37.1^{+11.4}_{-9.1}$
A689[a]	0.2793	841.1	$-184.4^{+30.2}_{-22.8}$	$397.8^{+186.2}_{-22.2}$	$9.11^{+2.98}_{-3.26}$	$0.41^{+0.54}_{-0.18}$	$0.691^{+0.143}_{-0.087}$	$21.6^{+6.2}_{-9.2}$
A697	0.2820	776.9	$5.8^{+10.8}_{-16.0}$	$-20.9^{+14.6}_{-14.1}$	$17.54^{+7.27}_{-6.16}$	$2.06^{+1.18}_{-0.72}$	$0.156^{+0.170}_{-0.155}$	$-52.1^{+141.8}_{-37.5}$
A750[a]	0.1630	835.5	$10.1^{+19.2}_{-14.7}$	$28.3^{+23.6}_{-21.0}$	$51.81^{+142.88}_{-10.60}$	$0.00^{+0.01}_{-0.00}$	$0.065^{+0.140}_{-0.011}$	$77.2^{+5.0}_{-3.8}$
A1835	0.2528	794.8	$-2.0^{+12.5}_{-15.9}$	$-0.9^{+16.7}_{-8.4}$	$11.60^{+5.15}_{-2.02}$	$3.66^{+1.05}_{-1.14}$	$0.420^{+0.120}_{-0.180}$	$45.5^{+10.1}_{-14.7}$
ZwCl1454	0.2578	745.9	$-24.3^{+6.8}_{-13.2}$	$81.7^{+16.7}_{-36.3}$	$4.06^{+2.88}_{-1.39}$	$2.68^{+1.81}_{-1.24}$	$0.568^{+0.106}_{-0.190}$	$-16.1^{+20.6}_{-15.7}$
ZwCl1459[a]	0.2897	977.9	$-22.3^{+5.6}_{-8.2}$	$-10.5^{+18.6}_{-17.5}$	$5.11^{+1.23}_{-1.62}$	$6.46^{+6.60}_{-1.55}$	$0.747^{+0.090}_{-0.105}$	$-9.6^{+5.6}_{-5.3}$
A2219	0.2281	753.0	$-9.7^{+13.0}_{-19.8}$	$5.9^{+7.3}_{-8.4}$	$6.65^{+2.69}_{-1.70}$	$8.99^{+6.33}_{-3.11}$	$0.705^{+0.043}_{-0.175}$	$-78.2^{+5.5}_{-8.0}$
RXJ1720[a]	0.1640	926.5	$-11.7^{+13.5}_{-6.9}$	$26.2^{+9.5}_{-12.6}$	$3.37^{+1.72}_{-0.99}$	$11.70^{+10.48}_{-4.29}$	$0.508^{+0.169}_{-0.309}$	$12.0^{+57.9}_{-10.0}$
A2261[a]	0.2240	906.1	$-18.3^{+11.7}_{-10.8}$	$17.1^{+10.7}_{-6.8}$	$10.45^{+2.83}_{-2.79}$	$5.16^{+2.08}_{-1.05}$	$0.255^{+0.156}_{-0.214}$	$64.9^{+31.3}_{-27.6}$
RXJ2129[a]	0.2350	755.4	$5.0^{+37.7}_{-22.8}$	$6.6^{+30.1}_{-17.2}$	$26.65^{+41.87}_{-8.52}$	$0.00^{+0.04}_{-0.00}$	$0.077^{+0.168}_{-0.023}$	$59.0^{+6.7}_{-7.2}$
A2390	0.2329	735.7	$-13.0^{+16.7}_{-15.4}$	$-16.5^{+15.6}_{-7.3}$	$7.27^{+3.26}_{-1.98}$	$6.39^{+4.29}_{-2.31}$	$0.598^{+0.083}_{-0.149}$	$-45.0^{+7.5}_{-13.5}$
A2485	0.2472	741.4	$-40.6^{+7.6}_{-6.9}$	$-4.0^{+20.6}_{-9.4}$	$2.29^{+1.33}_{-0.34}$	$15.25^{+6.40}_{-8.20}$	$0.808^{+0.015}_{-0.210}$	$-8.6^{+3.1}_{-5.9}$
A2631	0.2780	816.2	$1.6^{+10.5}_{-9.6}$	$-3.8^{+11.9}_{-8.3}$	$4.21^{+1.89}_{-1.18}$	$9.84^{+8.19}_{-4.52}$	$0.347^{+0.244}_{-0.344}$	$78.6^{+93.1}_{-44.5}$

[a] Removed for the analysis of cluster ellipticities, because the elliptical NFW model does not give an acceptable fit to the measurement (see text for more details).

$$C = C^{\rm shape} + C^{\rm lss}. \tag{10}$$

The intrinsic ellipticity noise is expected to be uncorrelated between different galaxies. Therefore, for the pixelised map, the shape noise covariance matrix has only diagonal terms:

$$\left[C^{\rm shape}\right]_{\alpha\beta,kl} = \delta^K_{\alpha\beta}\delta^K_{kl}\sigma^2_g(\boldsymbol{\theta}_k), \tag{11}$$

where $\delta^K_{\alpha\beta}$ or δ^K_{kl} denotes the Kronecker delta function, and σ_g is given by equation (3).

On the other hand, the covariance due to large-scale structure is given in Dodelson (2004) as (see also Hoekstra 2003)

$$\left[C^{\rm lss}\right]_{\alpha\beta,kl} = \xi_{\alpha\beta}(|\boldsymbol{\theta}_k - \boldsymbol{\theta}_l|), \tag{12}$$

where ξ is the cosmic shear correlation functions, and we have assumed that ξ is given as a function of the length of vector connecting the two points $\boldsymbol{\theta}_k$ and $\boldsymbol{\theta}_l$ due to the statistical isotropy of the Universe. Specifically, the shear correlation functions constructed from combinations of two shear components are expresses as

$$\xi_{11}(r) = (\cos 2\phi)^2 \xi_{++}(r) + (\sin 2\phi)^2 \xi_{\times\times}(r), \tag{13}$$
$$\xi_{22}(r) = (\sin 2\phi)^2 \xi_{++}(r) + (\cos 2\phi)^2 \xi_{\times\times}(r), \tag{14}$$
$$\xi_{12}(r) = \cos 2\phi \sin 2\phi \left[\xi_{++}(r) - \xi_{\times\times}(r)\right], \tag{15}$$

where $r = |\boldsymbol{\theta}_k - \boldsymbol{\theta}_l|$, ϕ is the position angle between the coordinate x-axis and the vector $\boldsymbol{\theta}_k - \boldsymbol{\theta}_l$, and ξ_{++} and $\xi_{\times\times}$ denote the tangential and cross component shear correlation functions (e.g., Bartelmann & Schneider 2001). For a given cosmological model, ξ_{++} and $\xi_{\times\times}$ are computed once the nonlinear mass power spectrum $P_\delta(k)$ and the mean source redshift are given. We assumed the concordance ΛCDM model (Komatsu et al. 2009) and used the fitting formula in Smith et al. (2003) to compute the nonlinear mass power spectrum.

Note that we ignored the error contribution arising from structures surrounding a cluster of interest. The surrounding structures cause the so-called two-halo contribution to the shearing effect on background galaxies (Sheldon et al. 2007a). However, we have checked that the two-halo term contribution is negligible over angular scales we have considered.

The dimension of the covariance matrix is given by twice of the number of pixels in the distortion map. For our case, $2 \times N_{\rm pixel} = 792$. On the other hand, the total number of parameters of an elliptical NFW model is 6, as described in §2.3. Therefore the degree of freedom of our 2D fitting is 786.

In order to find the best-fit model, we need to monitor the χ^2 values in 6-dimensional parameter space, which
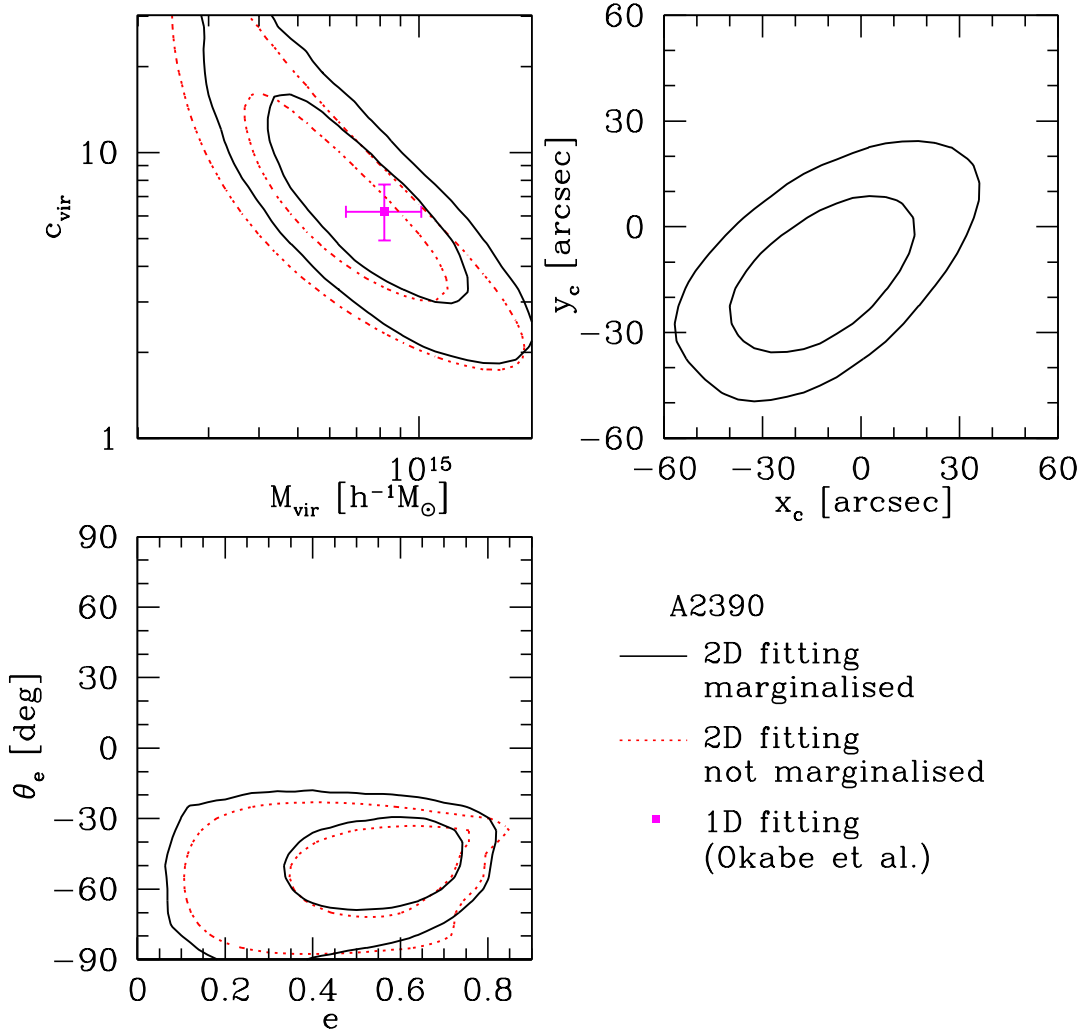
Figure 2. The fitting result for A2390. Solid contours show the 1σ and 2σ error contours, marginalised over other parameters, in each two-dimensional parameter space: the halo mass – concentration plane (*upper-left*), the halo centre offsets from the BCG position (*upper-right*), and the halo ellipticity and its position angle (*lower-left*). Dotted contours in the upper left panel show the 1σ ($\Delta\chi^2 = 2.3$) and 2σ ($\Delta\chi^2 = 6.17$) contours obtained assuming a spherical NFW model with the BCG position as the cluster centre (i.e., $x_c = y_c = e = 0$). The filled square with error bars is the result of 1D fitting by Okabe et al. (2010); the error bar appears to be small compared with the 1σ contour of the 2D result partly because those errors are obtained from the likelihood distribution projected onto one-dimensional space (i.e., $\Delta\chi^2 = 1$ for 1σ). Dotted contours in the lower left panel are those obtained when the mass and concentration parameters are fixed to the best-fit values and the centre fixed to the BCG position. The small differences between the solid and dotted contours in these two panels suggest that the halo ellipticity and centroid are not largely degenerate with the halo mass and concentration parameter.

is computationally time-consuming if using the grid based computation. We thus employ a Markov Chain Monte Carlo (MCMC) approach to explore the χ^2 surface, where a standard Metropolis-Hastings sampling with the multivariate-Gaussian as a proposal distribution is adopted. We restrict the range of the ellipticity to $0 < e < 0.9$, and the concentration as $c_{vir} < 40$. Beside these we do not add any prior information. The constraints on individual parameters are obtained by projecting the likelihood distributions (i.e., minimising χ^2) to the parameter space, including marginalisation over other parameter uncertainties.

3   RESULTS

3.1   Results for individual clusters

We study all the 25 clusters with colour information using the method described in §2. Table 1 summarises best-fit parameters for each cluster, which shows several interesting results. First, the 2D shear fitting can constrain the angular position of halo centre reasonably well with the typical accuracy of ~ 20 arcseconds ($\sim 50h^{-1}$ kpc) in radius. Secondly, the halo ellipticity is detected at a high significance for many of the clusters. Thirdly, the ability to constrain the cluster mass and concentration is not very degraded by including the cluster centre position and the halo ellipticity as new fitting parameters, if we compare the results with the

1D fitting results in Okabe et al. (2010). Below we explore these results in more detail.

In order to have a better understanding on parameter degeneracies, Figure 2 shows the projected constraint contours in each subspace of two parameters for A2390, one of the best-constrained clusters in our sample. We confirm that constraints on halo mass and concentration parameter are almost unchanged even if the other parameters are fixed to the best-fit values or to the values obtained from 1D fitting, i.e., assuming a spherical NFW model and the BCG position for the halo centre. Similarly, constraints on the halo ellipticity and its position angle is not degraded by fixing the other parameters. These results suggest that the ellipticity is degenerate neither with the cluster mass/concentration nor the cluster centre position. Therefore, by performing the full 2D fitting we gain additional information on cluster properties, which are not obtained from the conventional tangential shear profile, without degrading the ability to measure the radial mass profile.

Although most clusters are fitted reasonably well, some clusters have the large minimum χ^2 value compared with the degree-of-freedom, implying that an elliptical NFW model is not a good fit to the data. For instance, the best-fit models of A750 and RXJ2129 have very large $M_{\rm vir}$ and small $c_{\rm vir}$. The cluster centres are not constrained very well for A115 and A689 presumably because of their multimodal mass structures (see Okabe et al. 2010, for the reconstructed mass maps). In addition, for RXJ1720, A2261, and ZwCl1459, their reduced χ^2 values are large enough, $\chi^2_{\rm min}/786 \geqslant 1.146$, implying that the elliptical NFW model is rejected at 3σ level. In what follows, we remove these 7 clusters and analyse remaining 18 clusters (except for the analysis of the cluster centre presented in §3.3).

One may argue that removal of these clusters from the analysis might bias results on, e.g., cluster ellipticities which are thought to be correlated with the complexity of the internal mass distributions. However, note that the clusters excluded from the analysis do not necessarily have complicated internal mass distributions. We find that clusters sometimes yield poor fitting results simply because the data quality is not good enough for our six-parameter fitting. Indeed, some of the excluded clusters do have shallower depths or poorer seeing sizes than others. Another reason for poor fitting includes the projection of massive haloes along the line-of-sight, as in the case of A2261 (Okabe et al. 2010). Thus we expect that the bias caused by the exclusion is not so significant.

### 3.2 Distribution of halo ellipticities for 18 clusters

We combine the results of all the 18 clusters in order to confront the observed distribution of halo ellipticity parameter e with the CDM predictions. We construct the observed distribution as follows. As we have described so far, the halo ellipticity is constrained for each cluster, including marginalisation over other parameter uncertainties. However, the halo ellipticity is constrained having the projected errors. In order to properly take into account the errors, for each cluster we randomly select the likely true value of halo ellipticity assuming the posterior likelihood function of $p(e) \propto \exp(-\Delta\chi^2/2)$. We generate 10,000 realisations of the ellipticity measurement for each cluster, and combine
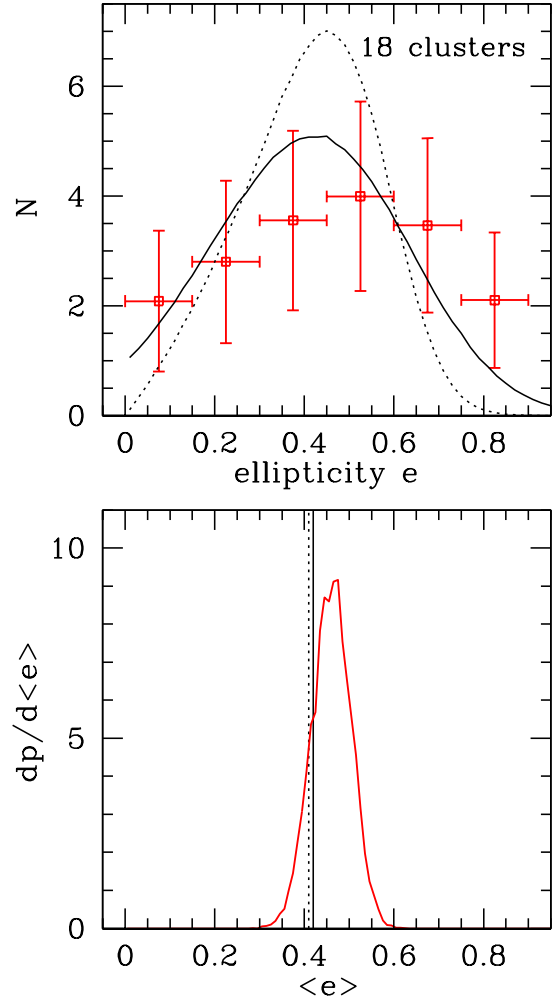
Figure 3. *Upper panel:* The distribution of the halo ellipticity e for 18 clusters. Note that the ellipticity is for the projected mass density (see equation [4]). The open squares with error bars show the observed distribution estimated from 10,000 Monte Carlo redistributions of the ellipticity parameters based on the posterior likelihood function of ellipticity for each cluster, where the error bars in each ellipticity bin denote the range including the 68 percentile of 10,000 realisations. Note that different bins are not independent but are correlated with each other. The solid curve is the theoretically-expected distribution of ellipticity based on a triaxial halo model of Jing & Suto (2002), computed adopting the cluster redshift of 0.23 and mass of $7 \times 10^{14} h^{-1} M_\odot$ (median redshift and mass for our cluster sample) and convolved with the Gaussian with $\sigma = 0.15$ which corresponds to a typical measurement uncertainty for our 2D shear fitting. The dotted curve shows the original theoretical prediction without the Gaussian convolution. *Lower panel:* The probability distribution of the mean ellipticity $\langle e \rangle$ for the 18 clusters. The vertical solid and dotted lines indicate the mean ellipticity expected from the triaxial halo model, with and without the Gaussian smoothing, respectively.

the results of all the clusters to estimate the mean number of clusters and its variance in each ellipticity bin.

Figure 3 shows the resulting distribution, where the error bar in each bin denotes the range including the 68 percentile of 10,000 realisations. The distribution can be compared with the CDM prediction of Jing & Suto (2002), which is derived by fitting dark haloes in N-body simula-
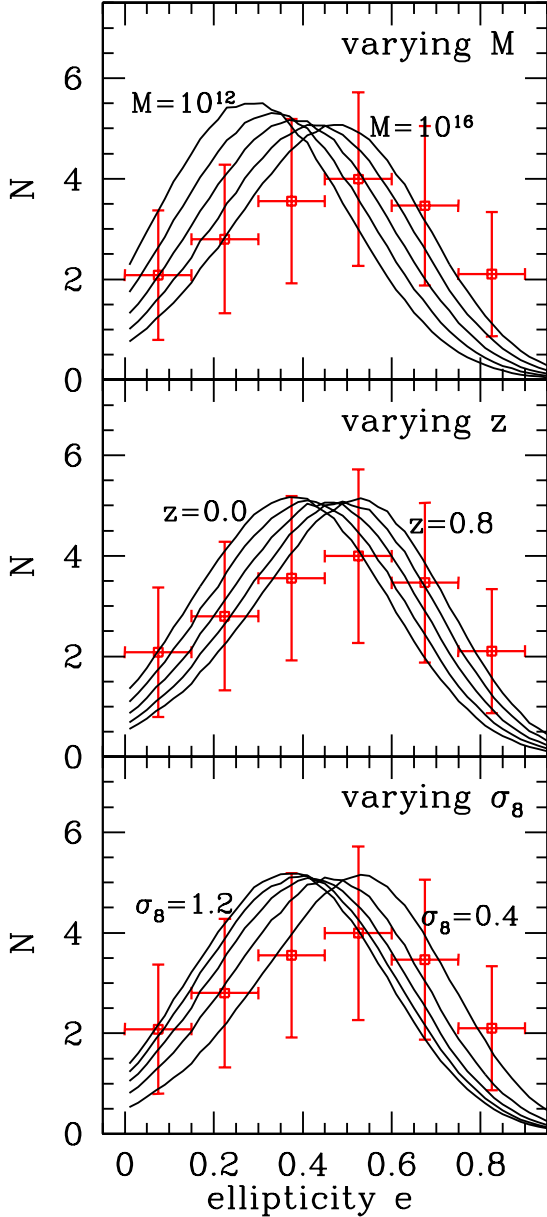
Figure 4. The solid curves in each panel show how the Gaussian-convolved CDM predictions (Jing & Suto 2002, see also Figure 3) for the halo ellipticity distribution change with halo mass (*upper*, from $M_{vir} = 10^{12} h^{-1} M_\odot$ to $10^{16} h^{-1} M_\odot$ with intervals of 1 dex), redshift (*middle*, from $z = 0$ to 0.8 with intervals of 0.2) and the normalisation parameter of primordial density fluctuations, σ_8 (*lower*, from $\sigma_8 = 0.4$ to 1.2 with intervals of 0.2). In each panel, except for varying parameter, the other parameters are fixed to the fiducial values. The square symbols with error bars are the measured distribution for 18 clusters shown in Figure 3.

tions with a triaxial NFW model. The CDM prediction in the Figure (dotted line) is computed as follows. First, again note that, if projecting the 3D triaxial model along the line-of-sight, the resulting mass distribution on the sky is exactly the same as that given in equation (4). Jing & Suto (2002) derived the probability distribution function of triaxial halo shapes (axis ratios) as a function of halo mass and cosmological models. Thus the theoretical prediction for the halo

ellipticity distribution of 2D mass density can be computed by projecting the triaxial halo model along arbitrary line-of-sight directions as described in detail in Oguri et al. (2003). It should be noted that the theoretical distribution rests on the implicit assumption that the cluster sample is unbiased in terms of both the shape and orientation. In the calculation, the concordance ΛCDM model is assumed, and the mass and redshift are fixed to the median mass and redshift of our cluster sample: $z = 0.23$ and $M_{vir} = 7 \times 10^{14} h^{-1} M_\odot$, respectively.

The plot shows that both observed and theoretical distributions peak at $e \sim 0.4 - 0.5$, but the observed distribution is significantly wider than the theoretical distribution. Apparently this is because of the measurement uncertainty which broadens the distribution. Thus a correction to the theoretical prediction is required to account for the measurement uncertainty. The solid curve shows the the theoretical distribution convolved with the Gaussian function with width of $\sigma = 0.15$, which corresponds to the typical uncertainty of the ellipticity measurement for our 2D shear fitting (see Table 1). Indeed, we find that the Gaussian-smoothed theoretical distribution better matches the observed distribution.

While the detection of non-zero halo ellipticity may be obvious from the distribution in Figure 3, we can quantify how well the elliptical model improves a fit to the 2D shear map compared to the spherical model by monitoring the χ^2 values in equation (9). The elliptical model improves the total χ^2 value for 18 clusters by $\Delta\chi^2 = 51$ compared with the spherical model with $e = 0$ fitted to the same 2D data, thereby representing the detection of an ellipticity at 7σ confidence level.

In the lower panel of Figure 3 the mean halo ellipticity, $\langle e \rangle$, for our sample of 18 clusters is compared with the theoretical prediction, where the width of the mean ellipticity distribution reflects the scatter among 10,000 realisations. The observed distribution has the mean ellipticity of $\langle e \rangle = 0.46 \pm 0.04$ (1σ) which is in excellent agreement with the triaxial model prediction, $\langle e \rangle = 0.42$ (0.41) with (without) the Gaussian smoothing.

The halo ellipticity depends on mass and redshift of clusters as well as on cosmological models. According to the CDM hierarchical structure formation scenario (Jing & Suto 2002), dynamically young haloes tend to have a more elongated shape at a given observed redshift. In other words, more massive haloes that have just recently formed tend to have a larger halo ellipticity. Figure 4 shows how the theoretically expected distribution of halo ellipticity depends on redshift and mass of haloes and one of cosmological parameters, σ_8, the normalisation of primordial density fluctuations. While the current measurement is not enough to discriminate the model differences due to a limited sample size, the Figure illustrates how measurements of halo ellipticities can potentially test the structure formation model.

3.3 Offset between lensing centre and BCG

In this section, we compare the positions of cluster centres inferred from weak lensing and from the brightest cluster galaxy(ies). Weak lensing provides a unique method to determine the centre position of dark matter distribution, and therefore is quite complementary to the optical
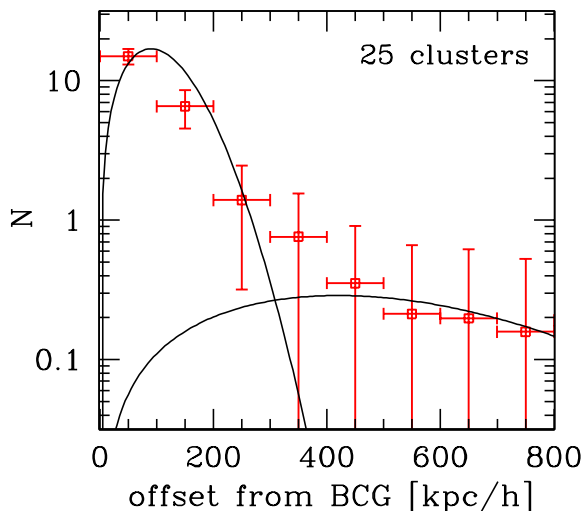
Figure 5. The distribution of the physical distance between the halo centre and the BCG position from the full sample of 25 clusters, obtained from 10,000 Monte Carlo redistributions computed as done in Figure 3. The solid curves show the two 2D Gaussian distributions with widths of $\sigma = 90h^{-1}$ kpc and $420h^{-1}$ kpc, respectively, where the Gaussian is given as $p(r) \propto r \exp[-r^2/(2\sigma^2)]$. The narrower Gaussian is obtained by fitting to the measured distribution. On the other hand, the broader Gaussian models a contribution with large offsets, motivated by the studies of Johnston et al. (2007). The width is kept fixed to $420h^{-1}$ kpc according to Johnston et al. (2007, see also text for the details), but its normalisation, treated as a free parameter, is estimated so as to best match the measured distribution.

(BCGs) and X-ray based methods. It should be also noted that a possible uncertainty in the centre position determination is currently one of the most important systematic sources in the stacked lensing analysis, cluster-background galaxy cross-correlation measurement (Johnston et al. 2007; Mandelbaum et al. 2010).

Our basic result, summarised in Table 1, is that the mass centres tend to be consistent with the locations of the BCGs. We find that mass centres are consistent with the BCG within 2σ level for most of the clusters. However, a possible significant deviation between the lensing and BCG centre positions is apparent for some of the clusters.

In the following we explore a possible signature of the large offset between BCG position and lensing centre in more detail. While we have worked mainly on a "clean" subsample of 18 clusters all of which are well fitted by an elliptical NFW model, here we analyse the full 25 clusters (all of which have colour information) in order to achieve a more unbiased study on the offset issue.

Figure 5 shows the lensing constrained distribution of the offset amount of the cluster centre from the BCG position for the 25 clusters. The distribution is computed from 10,000 Monte Carlo redistributions as done in Figure 3. First, the observed distribution generally shows that the BCG position is close to the cluster centre constrained from lensing. However, the distribution also indicates a tail at large offsets, although the significance is weak. To be more quantitative, the observed distribution is compared with a combination of the two 2D Gaussian distributions (solid curves) each of which is modeled as $p(r) \propto r \exp[-r^2/(2\sigma^2)]$

(r is the distance between the halo centre and BCG position). This form is motivated by the study in Johnston et al. (2007), where the cross-correlation weak lensing measurement between clusters and background galaxy images was studied in great detail using the SDSS data. They used the BCG position as the halo centre to carry out the stacked lensing analysis, and took into account the miscentring effect of the possible BCG offset by using the 2D Gaussian form with $\sigma = 420h^{-1}$kpc. This form was chosen based on their mock galaxy catalogues, from which they argued that clusters may be categorised into two populations, BCG-centred and BCG-offsetted clusters, and that the projected radial offset for the latter population can be described by the 2D Gaussian distribution. The two solid curves in Figure 5 shows the best-fit two 2D Gaussian distributions to the observed distribution, where the width of the broader Gaussian function is kept fixed to $\sigma = 420h^{-1}$ motivated by the study of Johnston et al. (2007). One can find that the best-fit curve fairly well matches the observed distribution. In addition, the relative strength of the two 2D Gaussian distributions implies a 10% fraction of BCG-offsetted clusters, which is again consistent with the assumption used in Johnston et al. (2007).

While the observed distribution is broadly consistent with the theoretical expectation, it is not clear whether the BCG offset is detected significantly, given the relatively large measurement uncertainties. In fact, the typical error on the mass centroid measurement is $\sigma \sim 50h^{-1}$ kpc, and there are a few clusters in the sample that have quite large errors, $\sigma > 100h^{-1}$ kpc, which are nonnegligible compared to the widths of the 2D Gaussian distributions discussed above. Thus, for more quantitative discussions on the distribution of BCG offset, we need a larger sample of weak lensing clusters.

We also compare the offsets between BCGs and mass centroids from weak lensing with those between BCGs and X-ray centres derived by Sanderson et al. (2009) using *Chandra* X-ray images. We do not find any significant correlation between these offsets. One of the reasons is that offsets between BCGs and X-ray centres for our cluster sample are typically much smaller than the accuracy of mass centroid determinations from weak lensing. We leave more detailed comparisons with X-ray data in future work.

3.4 Comparison with member galaxy distributions

It is often assumed that the distribution of cluster member galaxies follows the mass distribution (e.g., Evans & Bridle 2009). We test this assumption based on our 2D shear fitting.

First we defined member galaxies as galaxies sitting around the cluster red-sequence locus in the colour-magnitude diagram with their red-band magnitudes brighter than 22 mag (see also Okabe et al. 2010). We fit the number distribution of member galaxies by assuming an elliptical power-law profile. In fitting we fix the centre to the best-fit centre of the mass distribution from 2D shear fitting. Since the member galaxy catalogue is expected to be more or less contaminated by field galaxies, we add the constant density component in addition to the primary power-law component. Thus the parameters of our fitting is the slope and normalisation of the power-law profile, the ellipticity and position angle, and the constant density component. The fitting is performed in the same $20' \times 20'$ region as in the
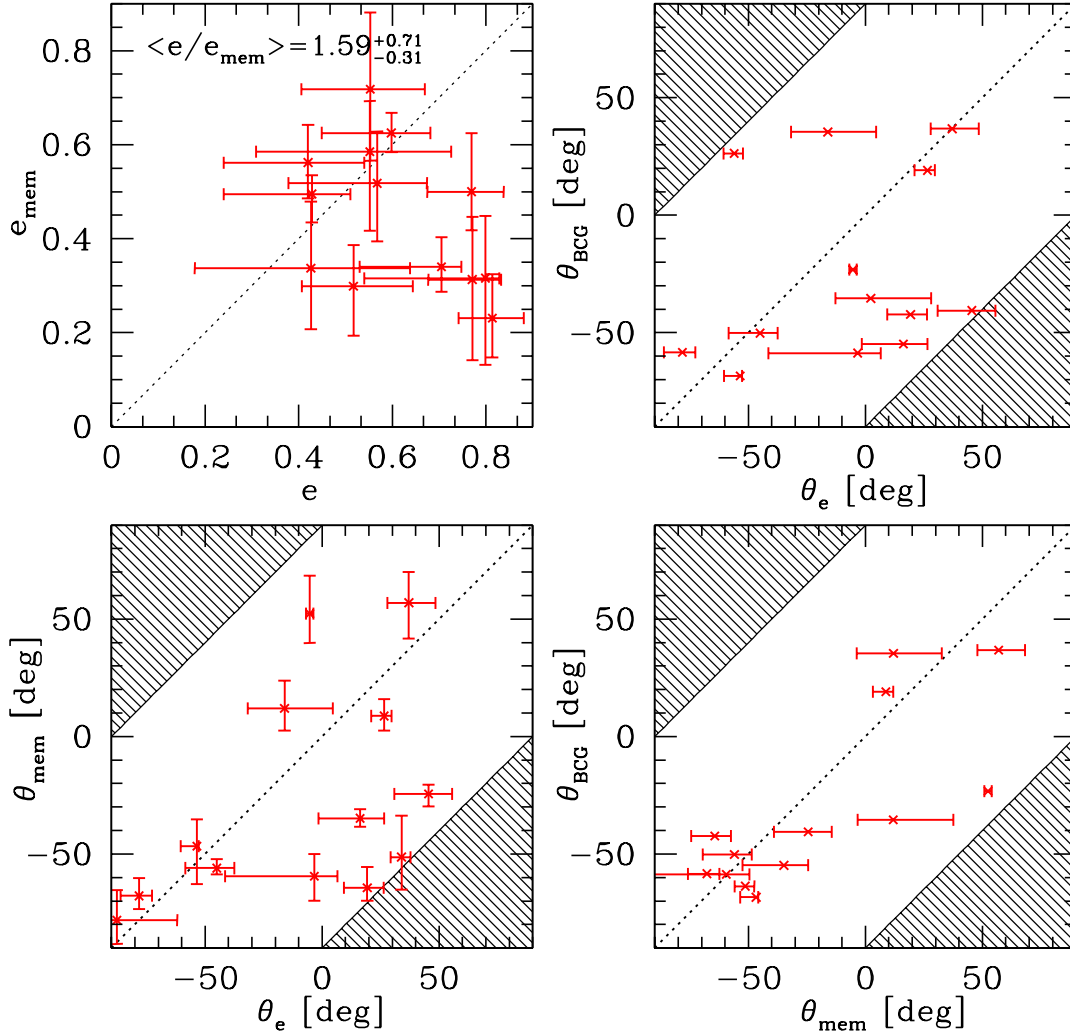
Figure 6. Comparisons between the mass and member galaxy distributions. *Upper-left panel:* The comparison of the mass ellipticity e with the ellipticity of the member galaxy distribution, $e_{\rm mem}$, for a sample of 13 clusters whose position angles are well constrained. The dotted line indicates $e = e_{\rm mem}$. The ellipticity ratio among the cluster sample is $\langle e/e_{\rm mem} \rangle = 1.59^{+0.71}_{-0.31}$, showing no strong correlation. *Lower-left panel:* The position angles of the mass distribution from 2D shear fitting, θ_e, are compared with the position angles of member galaxy distributions, $\theta_{\rm mem}$. The dotted line shows the case of the perfect alignment, $\theta_e = \theta_{\rm mem}$. The shaded corners have misalignments greater than 90° and therefore are excluded (for some clusters both the position angles are shifted by 90 degree to fit in the proper region). *Upper-right panel:* Comparison between θ_e and the BCG position angle $\theta_{\rm BCG}$. *Lower-right panel:* Comparison between $\theta_{\rm mem}$ and $\theta_{\rm BCG}$.

shear fitting for each cluster. The result is summarised in Table 2. The table also lists the shape and orientations of BCG for each cluster, which is obtained from the SExtractor output (Bertin & Arnouts 1996). The measurement errors for BCG shapes are negligibly small, although the orientations of the BCGs may slightly depend on the radius where it is determined.

Figure 6 compares the 2D shapes of mass and member galaxy distributions. Here we restrict our analysis to a subsample of 13 clusters whose position angles are constrained reasonably well in our fitting. First, while ellipticities mass and member galaxies are consistent with each other for roughly half of the clusters, overall we do not see any strong correlation between the ellipticities. Although we find that the mass ellipticity tend to be larger than the ellipticity of member galaxy distributions, this may be as-

cribed to the selection effect: We only consider clusters with well-determined position angles from shear fitting, which preferentially selects clusters with large mass ellipticities, as is clear from Figure 6. Is is also possible that our ellipticity measurement of the member galaxy distribution is biased because of the inclusion of photometrically selected red-sequence galaxies only and the contamination by field galaxies.

Although we see some correlation between position angles of mass and member galaxies distributions, the alignment is not very strong. In some case the position angles are similar between the mass and member galaxy distributions, but there are cases that the orientations of the member galaxy distributions are significantly different from those of the mass distributions. The results are qualitatively similar even if we adopt orientations of BCGs. On the other hand,

Table 2. The shapes and orientations of member galaxies and BCGs. The errors are the marginalised 1σ errors (see text for the details).

Name	$e_{\rm mem}$	$\theta_{\rm mem}$ (deg)	$e_{\rm BCG}$	$\theta_{\rm BCG}$ (deg)
A68	$0.585^{+0.108}_{-0.168}$	$-59.5^{+9.4}_{-10.4}$	0.326	-58.7
A115	$0.298^{+0.132}_{-0.206}$	$17.2^{+27.0}_{-10.6}$	0.268	-30.9
A209	$0.495^{+0.040}_{-0.060}$	$-34.8^{+3.9}_{-3.6}$	0.539	-54.8
RXJ0142	$0.316^{+0.132}_{-0.184}$	$-46.7^{+11.5}_{-16.1}$	0.341	-68.4
A267	$0.500^{+0.125}_{-0.082}$	$8.7^{+7.2}_{-6.1}$	0.507	19.1
A291	$0.313^{+0.133}_{-0.172}$	$-51.3^{+17.6}_{-13.8}$	0.121	-63.7
A383	$0.231^{+0.093}_{-0.084}$	$52.3^{+16.1}_{-12.5}$	0.085	-23.2
A521	$0.308^{+0.076}_{-0.069}$	$-40.7^{+8.9}_{-9.1}$	0.262	-44.1
A586	$0.337^{+0.142}_{-0.130}$	$-78.2^{+12.7}_{-10.1}$	0.157	54.6
ZwCl0740	$0.718^{+0.163}_{-0.152}$	$-64.4^{+8.9}_{-5.4}$	0.233	-42.3
ZwCl0823	$0.342^{+0.207}_{-0.248}$	$-25.9^{+32.7}_{-14.7}$	0.303	-23.7
A611	$0.299^{+0.087}_{-0.105}$	$56.9^{+13.1}_{-15.2}$	0.220	36.8
A689	$0.900^{+0.000}_{-0.013}$	$8.9^{+3.0}_{-1.5}$	0.471	38.9
A697	$0.499^{+0.072}_{-0.086}$	$-38.8^{+3.6}_{-4.1}$	0.278	-14.0
A750	$0.229^{+0.092}_{-0.064}$	$-81.5^{+12.4}_{-8.5}$	0.364	-41.2
A1835	$0.562^{+0.080}_{-0.076}$	$-24.4^{+4.0}_{-5.3}$	0.355	-40.6
ZwCl1454	$0.518^{+0.110}_{-0.124}$	$12.0^{+11.8}_{-9.4}$	0.302	35.4
ZwCl1459	$0.209^{+0.171}_{-0.175}$	$43.4^{+30.7}_{-20.8}$	0.360	-83.8
A2219	$0.340^{+0.063}_{-0.053}$	$-67.8^{+7.5}_{-5.6}$	0.301	-58.4
RXJ1720	$0.473^{+0.083}_{-0.147}$	$19.7^{+8.8}_{-10.4}$	0.189	29.5
A2261	$0.407^{+0.073}_{-0.066}$	$48.9^{+6.9}_{-3.8}$	0.185	-1.1
RXJ2129	$0.352^{+0.064}_{-0.075}$	$67.3^{+8.7}_{-8.1}$	0.443	68.1
A2390	$0.625^{+0.043}_{-0.041}$	$-56.0^{+3.8}_{-2.6}$	0.232	-50.2
A2485	$0.186^{+0.146}_{-0.185}$	$-36.1^{+124.6}_{-51.0}$	0.263	64.9
A2631	$0.562^{+0.078}_{-0.096}$	$61.6^{+4.7}_{-4.0}$	0.316	81.1

the distributions of member galaxies and the orientations of BCGs are aligned better with each other.

To understand the origin of the misalignment, we visually inspect mass maps of clusters which show large misalignments, and find that many of them appear to possess significant substructures (e.g., A68, A209, A291, A383). However, it is not obvious whether these substructures cause the misalignment directly, or clusters with significant substructures are dynamically young and have complicated internal mass distributions and larger fractions of blue member galaxies which might cause the misalignments. Indeed, our simple simulations in Appendix A indicate that massive subpeaks do not have significant impact on the measurements of 2D cluster shapes unless their masses are approximately more than 20% of the main halo. In either case, our results imply that the non-sphericity of halo cannot be reliably explored using the galaxy distribution or even using the stacked two-dimensional lensing technique which assumes the alignment of galaxy and dark matter distribution (Evans & Bridle 2009).

3.5 Cluster ellipticities from other techniques

While our weak lensing technique provides a direct detection of the cluster mass ellipticity over the entire cluster region, signatures of cluster non-sphericity have been obtained using other techniques as well. Here we review some of the previous results in comparison with our results.

One straightforward way to study the shape of clusters is to see the distribution of member galaxies (Rhee et al. 1991; de Theije et al. 1995; Adami et al. 1998; Strazzullo et al. 2005). Indeed ellipticities of $\sim 0.2 - 0.5$ have been detected for a number of clusters. While member galaxies (stars) are collisionless and therefore their spatial distribution is naively expected to follow the underlying dark matter distribution, the complicated galaxy formation physics makes it rather difficult to predict theoretically how these distributions are in fact connected. On the other hand, measurements of cluster shapes from X-ray (McMillan et al. 1989; Mohr et al. 1995; Buote & Tsai 1995; Kolokotronis et al. 2001; Flores et al. 2007) may be easier to interpret, because one can connect the distribution of X-ray emitting hot gas with the underlying dark matter distribution under the assumption of the hydrostatic equilibrium (e.g., Lee & Suto 2003; Wang & Fan 2004), although the assumption sometimes does not hold – an extreme example is the bullet cluster (Clowe et al. 2006). The typical observed ellipticities of X-ray surface brightnesses of $e \sim 0.2$ are smaller than our measurement from weak lensing, which is in fact expected because under the hydrostatic equilibrium assumption the isodensity surface of the intra-cluster gas follows the iso-potential surface, which is generally rounder than the dark matter distribution (Buote & Canizares 1992). Recently, Kawahara (2010) derived the axis ratio distribution of X-ray clusters using XMM-Newton data. It was claimed that, by taking into account the apparent rounder shape in the X-ray image, the distribution agrees well with the theoretical prediction based on the triaxial dark matter halo and hydrostatic equilibrium, which therefore seems consistent with our finding.

The dark matter distribution can also be studied by strong gravitational lensing. While the necessity of large ellipticities in some individual cluster strong lensing mass models has long been recognised (e.g., Miralda-Escude 1995), recently Richard et al. (2010) presented a strong lens analysis of 20 LoCuSS clusters, and derived the mean ellipticity of $\langle e \rangle \sim 0.4$, in broad agreement with our result. One possible caveat is that the parameter constraints are highly degenerated due to the nature of complex nonlinear fitting in the strong lensing region. In addition, the ellipticity constraint from strong lensing is on much inner region ($\lesssim 100$ kpc in radius) than our weak lensing measurements, where the mass distribution may be significantly affected by various baryonic effects such as radiative cooling and the dynamical interaction between dark matter and central galaxies. Nevertheless, strong lensing constraints are of great interest because of a natural prediction of the CDM model that the halo ellipticity and position angle slightly changes with cluster centric radii due to the collision-less nature of dark matter (Jing & Suto 2002). Therefore the combination of strong lensing and weak lensing constraints may allow a more quantitative test on these scenarios. Indeed we are planning to conduct combined strong and weak lensing analysis for our LoCuSS cluster sample, which will be presented elsewhere (G. Smith et al., in preparation).

3.6 Ellipticity of galaxy-scale haloes

Both the surface brightness distribution (e.g., Sheth et al. 2003; Choi et al. 2007) and strong lens mass modeling (e.g.,
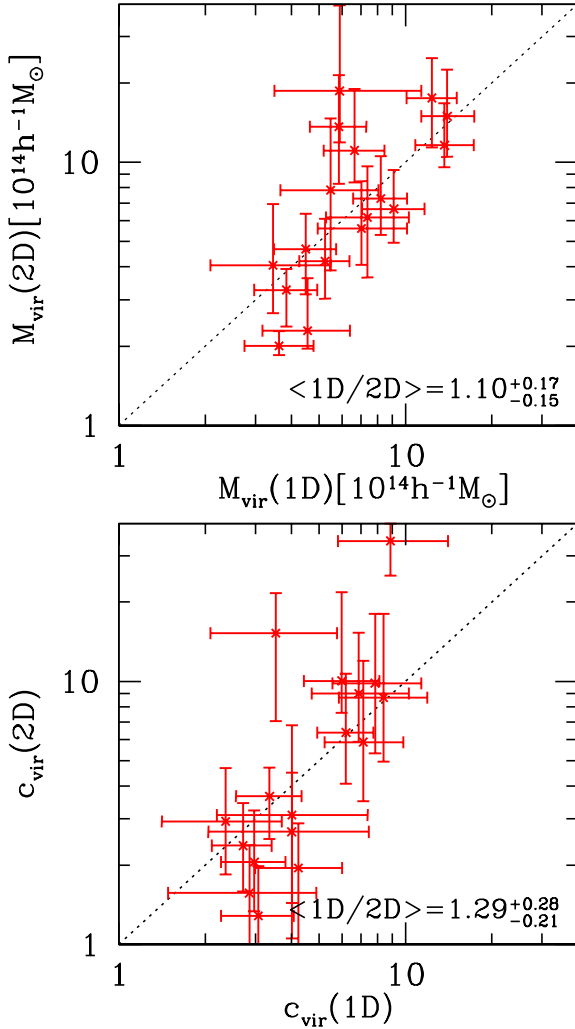
Figure 7. The upper panel compares the best-fit mass parameters ($M_{\rm vir}$) from the 1D shear fitting (Okabe et al. 2010) and the 2D fitting in this paper, while the lower panel show the concentration parameters ($c_{\rm vir}$). The mean ratios are $\langle M_{\rm vir}(1{\rm D})/M_{\rm vir}(2{\rm D})\rangle = 1.10^{+0.17}_{-0.15}$ and $\langle c_{\rm vir}(1{\rm D})/c_{\rm vir}(2{\rm D})\rangle = 1.29^{+0.28}_{-0.21}$, respectively.

Keeton et al. 1998; Koopmans et al. 2006) indicate that the mean ellipticity of $\langle e \rangle \sim 0.2 - 0.3$ near the core of early-type galaxies. The standard hierarchical structure formation scenario suggests that more massive haloes are more dynamically young and therefore are more elongated (e.g., Jing & Suto 2002). Thus the smaller ellipticities of early-type galaxies than massive clusters are qualitatively in good agreement with the theoretical expectation.

However, the central mass distribution of early-type galaxies is more likely affected by radiative cooling and star formation of baryons (Kazantzidis et al. 2004; Tissera et al. 2010). Constraints on the shape of galaxy-scale haloes at outer regions, measured by stacked weak lensing technique, are somewhat controversial (Hoekstra et al. 2004; Mandelbaum et al. 2006a; Parker et al. 2007).

3.7   Comparison with 1D tangential shear fitting

The conventional way to extract cluster mass and concentration from weak lensing data is to fit a 1D (i.e., spherical) mass model to the 1D tangential shear profile (e.g., Okabe et al. 2010). We can therefore now compare the results of our 2D model fits to the 2D shear data with those of 1D models obtained by Okabe et al. (2010). For instance, if an elliptical halo model is a better description of real clusters than a spherical one and if the lensing data has the ability to discriminate these two models, the 2D shear fitting method can bring a more reliable, unbiased estimate on cluster parameters, which is particularly important for cluster cosmology experiments aimed at constraining dark energy. In the following we focus on the subsample of 17 clusters, the "good" 18 clusters but excluding the cluster ZwCl0823 because ZwCl0823 does not allow a good 1D shear fitting due to the complex, non-spherical mass distribution (Okabe et al. 2010).

Figure 7 compares the best-fit mass/concentration parameters obtained from the 1D and 2D fitting methods. The 1D and 2D results agree reasonably well. In particular, the virial masses $M_{\rm vir}$ from 1D and 2D fitting are well consistent with each other within 1σ statistical errors. With the current sample size we cannot conclude that there is a systematic bias in the different cluster mass estimates. The possible deviation, $\langle M(1{\rm D})/M(2{\rm D})\rangle = 1.10^{+0.17}_{-0.15}$, averaged over the 18 clusters is within the 1σ scatter.

On the other hand, the concentration parameters are more scattered, and the average ratio of $\langle c_{\rm vir}(1{\rm D})/c_{\rm vir}(2{\rm D})\rangle = 1.29^{+0.28}_{-0.21}$ deviate from unity with 1σ confidence level. This is probably related with the fact that the determination of concentration parameter is more difficult and is easily affected by various uncertainties such as the fitting region and cluster centres. In fact, the fitting regions are slightly different between Okabe et al. (2010) and our 2D analysis, which can cause such slight discrepancy.

We note that lensing determinations of $M_{\rm vir}$ and $c_{\rm vir}$ are sometimes highly degenerate. Thus slightly different fitting method can result in large different in $M_{\rm vir}$ and c just because the best-fit value moves along this degeneracy direction. Indeed, we compare 1D and 2D results for individual clusters, and find that cluster with $M_{\rm vir}(1{\rm D}) > M_{\rm vir}(2{\rm D})$ tend to have $c_{\rm vir}(1{\rm D}) < c_{\rm vir}(2{\rm D})$, being consistent with the above picture, which also explains the relatively large scatter between 1D and 2D results seen in Figure 7.

In Appendix B we also show the 2D fitting results for M_{500} and c_{500} defined by the overdensity $\Delta = 500$, which is more relevant when comparing the lensing results with the X-ray derived mass estimates (e.g. Vikhlinin et al. 2009).

3.8   Effect of large-scale structure

Another new result of this paper is that we properly took into account the effect of cosmic shear contamination due to large-scale structure on the estimation of cluster parameters on individual cluster basis (see around equation [10] for the details). While Hoekstra (2003) theoretically estimated that the cosmic shear contributes to the error covariance matrix (see also Dodelson 2004), the effect has been ignored in most of previous cluster lensing studies, which suggests
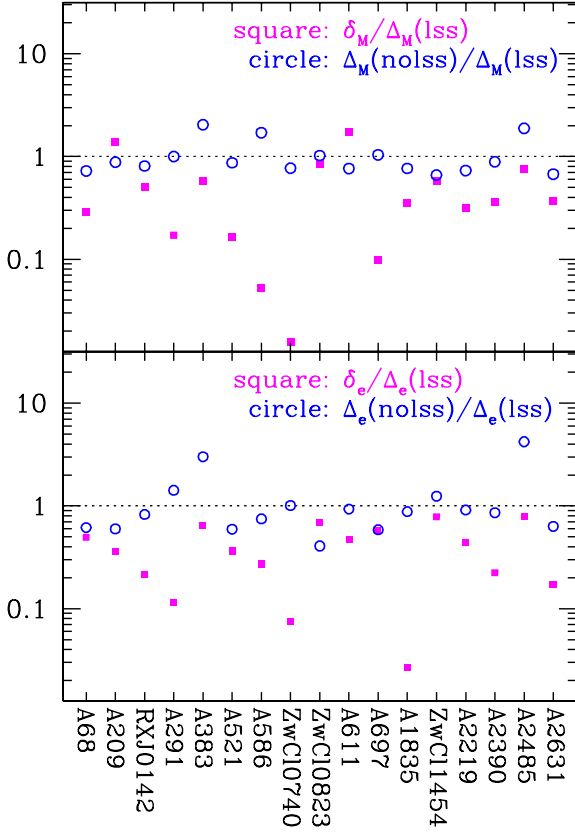
Figure 8. Shown is how the cosmic shear contamination (C^{lss}) in the error covariance matrix in the 2D shear fitting (see equation [10]) affects estimations of the mass (*upper panel*) and the halo ellipticity (*lower*). We quantify this effect by the following two parameters; the bias $\delta_p \equiv |p(\text{lss}) - p(\text{nolss})| / \sigma_p(\text{lss})$, where p and σ_p are the best-fit parameters (mass or ellipticity) and the marginalised 1σ errors computed with and without the contamination C^{lss}, and the fractional errors, $\Delta_p \equiv \sigma_p/p$, for both the results with and without C^{lss}. The ratio $\delta_p/\Delta_p(\text{lss})$, shown by the square symbols, quantifies how much the best-fit parameters are shifted compared with the statistical errors. The open circles show $\Delta_p(\text{nolss})/\Delta_p(\text{lss})$ which indicate the change of measurement errors due to C^{lss}.

that previous work may have underestimated errors on mass estimates.

Figure 8 studies a bias in the best-fit parameters as well as a change of the parameter estimation accuracy when the cosmic shear contamination in the covariance matrix (C^{lss} in equation [10]) is included or ignored. Here we consider 17 clusters, the fiducial 18 clusters minus A267, because A267 is not fitted very well without the C^{lss} term in the covariance matrix. First, the Figure shows that the parameter accuracies are little changed by including C^{lss}, while a few clusters show a large degradation. Thus the degradation amount is not as large as that claimed in Hoekstra (2003), presumably because the number density of our background galaxy sample ("red+blue" galaxies) is much smaller than that assumed in Hoekstra (2003) and therefore the shot noise is a more dominant source of the measurement errors than the cosmic shear contamination. The best-fit parameters are not largely biased by including C^{lss}, but are in general consistent with each other within statistical uncertainties.
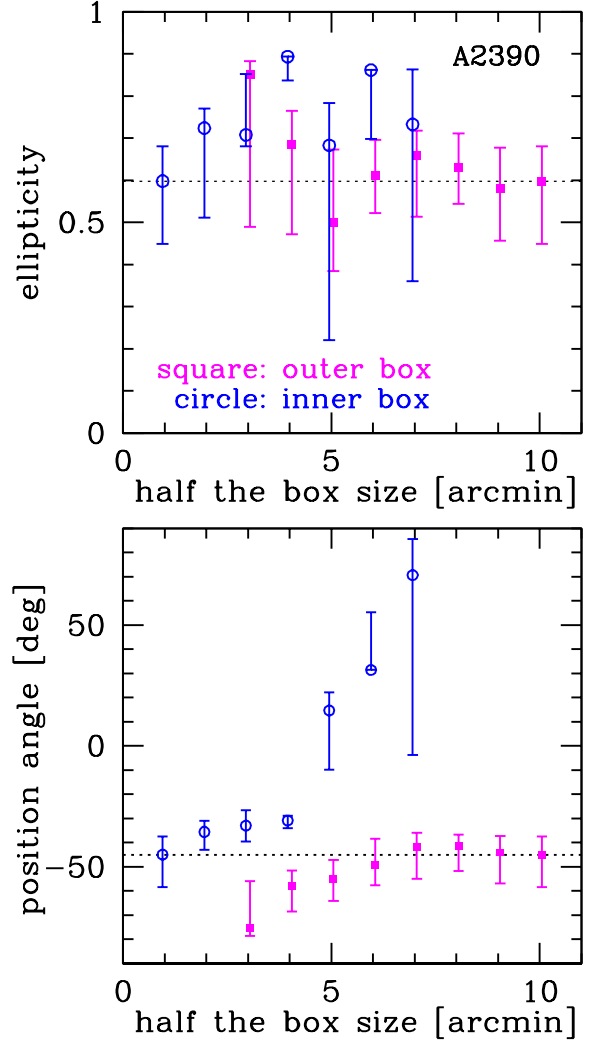
Figure 9. The best-fit halo ellipticities (*upper*) and position angles (*lower*) with their marginalised 1σ errors for different fitting regions, for the case of A2390. We change the outer box size while fixing the inner box size (*square symbols*) or vice versa (*circles*). Note that shear fitting is performed in the range inside the outer box and outside the inner box, around the coordinate origin (taken to be the BCG position). The ellipticities are plotted as a function of half the box size, which very roughly corresponds to the radius from the cluster centre.

4   DISCUSSIONS ON SYSTEMATIC ERRORS

In this section we discuss possible systematic errors inherent in our weak lensing measurements.

4.1   Constraining cluster region for the halo ellipticity

Our analysis has so far used the square region of $20' \times 20'$ centred at the BCG position, but excluding the inner region of $2' \times 2'$ (see § 2.2). In order to obtain a better understanding of the origin of the constraints on the ellipticity, we check the dependence of the result on the cluster fitting region. Specifically, we change the outer and inner boundary box sizes to see how the constraint on halo ellipticity

changes. Figure 9 shows the result for the cluster A2390. When the outer box size is changed with fixed inner boundary, the best-fit ellipticity and its error are little changed as long as the region with $\lesssim 5'$ is included. On the other hand, with increasing the inner box size, but keeping the outer boundary, the resulting ellipticity deviates from the original best-fit value at $\gtrsim 3'$. The result indicates that the most important radius for determining cluster ellipticities is $3' \lesssim r \lesssim 5'$ ($\sim 400 - 800 h^{-1}$ kpc) where the weak lensing signals tend to have maximum signal-to-noise ratios given the cluster lensing signal and the shot noise due to the finite number density of background galaxies in Subaru data (Okabe et al. 2010). This trend is generally true for all the "good" 18 clusters.

The Figure indicates that the best-fit position angle can shift by changing the fitting region. This may be an indicative of the twist of isodensity contours seen in N-body simulations (Jing & Suto 2002), although non-local nature of weak lensing shear makes the interpretation somewhat difficult.

For more definiteness, we check the stability of our result on the cluster ellipticity adopting two different boundary sizes. One is the smaller outer boundary box size of $10' \times 10'$, and the other is the larger inner box size of $4' \times 4'$. We repeat the analysis for these two cases, and obtain the mean ellipticities of $\langle e \rangle = 0.47 \pm 0.04$ and 0.50 ± 0.05, respectively, which are quite consistent with the main result presented in §3.2. This indicates that our results are not dependent on the specific choice of the fitting boundaries very much.

4.2 Dilution effect

If the background galaxy sample for weak lensing analysis contains a significant fraction of cluster member galaxies, it dilutes weak lensing signals (Broadhurst et al. 2005; Medezinski et al. 2007). This dilution effect becomes more pronounced near the cluster centre where the number density of cluster member galaxies is higher. Since weak lensing shear is non-local, it decreases very slowly with increasing radius, leading to much smaller dilution effect at outer radii. To check the impact of the dilution effect, we repeat the same 2D shear fitting for the "faint" galaxy sample (galaxies selected only by the magnitude cut, without any selection from the colour) instead of "red+blue" galaxy sample (see Okabe et al. 2010, for more detailed definitions of these samples). We find that the resulting mean ellipticity from the faint galaxy catalogue, which is much more significantly contaminated by the cluster member galaxies, is $\langle e \rangle = 0.44 \pm 0.04$. The result is fully consistent with the result adopting "red+blue" sample, which indicates that the dilution effect is not very important in constraining cluster ellipticities. This is probably because the ellipticity is sensitive mainly to the two-dimensional shear pattern rather than shear amplitudes which are more affected by the dilution. Note that profile parameters, cluster mass and concentration, are sensitive to the shear amplitudes, therefore more affected by the dilution (Okabe et al. 2010).

4.3 Effect of subpeaks on the ellipticity measurement

One may argue that the large cluster ellipticity we measured is an artifact due to the projection effect of foreground/background structures or prominent substructures in the cluster region, which may cause an apparent large elongation in the mass distribution for the cluster region. To explore this possibility, we visually inspect mass and luminosity density maps for our sample of clusters (Okabe et al. 2010). Among the 18 clusters used for the statistical analysis of the cluster shape, we find that A267, ZwCl0823, A697, and A2631 have probable subpeaks which might affect our ellipticity measurements. We remove these 4 clusters, redo analysis, and find the mean ellipticity to be $\langle e \rangle = 0.48 \pm 0.05$, in good agreement with our main result.

While the effect of cluster substructures on the cluster shape measurement turns out to be not so significant compared with the statistical measurement uncertainty (Appendix A), we also test this by further removing A68, A209, A291, and A383, which show large misalignments between the distributions of dark matter and member galaxies and appear to possess large substructures (see §3.4). The mean ellipticity for the remaining 10 clusters is $\langle e \rangle = 0.46 \pm 0.06$, which is still quite consistent with our main result. Therefore, together with the result of simple simulations in Appendix A, we conclude that the projection effect or the effect of cluster substructures are negligible.

5 CONCLUSION

In this paper, we have presented a systematic study to explore the ellipticity of cluster mass distribution directly from the 2D pattern of weak lensing distortion measured from background galaxy images. Our sample of high quality Subaru/Suprime-cam images for 25 X-ray selected clusters (Okabe et al. 2010) has enabled reliable statistical studies of dark matter distributions in massive cluster in great details. We developed a method of comparing the measured distortion patter with the prediction computed from an elliptical NFW model, where the halo ellipticity is modeled in the projected mass density and the resulting shear field is computed by solving the 2D Poisson equation (see § 2.3). Also notable is our method properly includes the error covariance matrix arising from the shot noise due to intrinsic ellipticities as well as the cosmic shear contamination due to large scale structures that are at different redshifts, but along the same line of sight to the cluster (see § 2.4). By conducting the 2D shear fitting, we can extract information on the shape of dark matter distribution in the cluster region in addition to the cluster mass and the profile parameters (halo concentration). We have shown several interesting results, and our findings are summarised as follows.

From a sample of 18 clusters, we have determined the mean ellipticity of the dark matter distribution to be $\langle e \rangle = \langle 1 - b/a \rangle = 0.46 \pm 0.04$ (1σ), in excellent agreement with the prediction of the triaxial halo model by Jing & Suto (2002) (see Figure 3). By comparing the results with the fitting results obtained from the spherical NFW model ($e = 0$), we concluded that the ellipticity is detected at 7σ confidence level, which has been achieved without assuming the location of mass peaks and the alignment between mass and

light. Interestingly, we found that the constraints on halo ellipticity parameters are not largely degenerated with halo mass and concentration, implying that the halo ellipticity is constrained mainly from the 2D shear pattern rather than the shear amplitudes (see Figure 2).

According to the CDM predictions, dynamically young and more massive haloes tend to have larger ellipticities. That is, the halo ellipticity should depend on redshift and mass of clusters as well as on cosmological models. However, our results are not sufficient to discriminate the model differences due to the limited size of our cluster sample (see Figure 4).

It appears that our results are robust against several possible systematics, such as the dilution effect, substructures in clusters, and projections of other haloes along the line-of-sight. For masses and concentrations, we find no significant systematic differences between the 1D and 2D analysis (see Figure 7). The mass centroid positions constrained from weak lensing is typically consistent with the BCG positions with a typical accuracy of ~ 20 arcseconds ($\sim 50h^{-1}$ kpc), although there are a few clusters that show significant offsets (see Figure 5). We have found that the correlation between the orientations of the dark matter distribution and cluster member galaxy distributions is not very strong, possibly because of the limitation of our member galaxy sample which is defined photometrically using only two-band images. Therefore it is of interest to repeat the analysis using spectroscopically confirmed cluster members.

Overall, our results demonstrate the importance of analysing the full 2D distributions of cluster weak lensing data. The 2D shear map contains much richer information than azimuthally-averaged 1D tangential shear profiles which have been a main focus in most of previous studies. Direct tests of dark matter distributions should grow its importance in the era of wide-field imaging surveys which will bring an exciting opportunity to explore the full use of the method presented in this paper in order to obtain stringent, quantitative constraints on the collisionless CDM scenario on small non-linear scales.

REFERENCES

Adami C., Mazure A., Katgert P., Biviano A., 1998, A&A, 336, 63

Allgood B., Flores R. A., Primack J. R., Kravtsov A. V., Wechsler R. H., Faltenbacher A., Bullock J. S., 2006, MNRAS, 367, 1781

Bahcall N. A., Cen R., 1993, ApJ, 407, L49

Bahcall N. A., Bode P., 2003, ApJ, 588, L1

Bardeau S., Soucail G., Kneib J.-P., Czoske O., Ebeling H., Hudelot P., Smail I., Smith G. P., 2007, A&A, 470, 449

Bartelmann M., 1996, A&A, 313, 697

Bartelmann M., Schneider P., 2001, PhR, 340, 291

Bertin E., Arnouts S., 1996, A&AS, 117, 393

Borgani S., et al., 2001, ApJ, 561, 13

Böhringer H., et al., 2004, A&A, 425, 367

Buote D. A., Canizares C. R., 1992, ApJ, 400, 385

Buote D. A., Tsai J. C., 1995, ApJ, 439, 29

Bradač M., Allen S. W., Treu T., Ebeling H., Massey R., Morris R. G., von der Linden A., Applegate D., 2008, ApJ, 687, 959

Broadhurst T., Takada M., Umetsu K., Kong X., Arimoto N., Chiba M., Futamase T., 2005, ApJ, 619, L143

Broadhurst T., Umetsu K., Medezinski E., Oguri M., Rephaeli Y., 2008, ApJ, 685, L9

Choi Y.-Y., Park C., Vogeley M. S., 2007, ApJ, 658, 884

Clowe D., Bradač M., Gonzalez A. H., Markevitch M., Randall S. W., Jones C., Zaritsky D., 2006, ApJ, 648, L109

Corless V. L., King L. J., Clowe D., 2009, MNRAS, 393, 1235

Cypriano E. S., Sodré L. J., Kneib J.-P., Campusano L. E., 2004, ApJ, 613, 95

Dahle H., 2006, ApJ, 653, 954

de Theije P. A. M., Katgert P., van Kampen E., 1995, MNRAS, 273, 30

Deb S., Goldberg D. M., Heymans C., Morandi A., 2010, ApJ, submitted (arXiv:0912.4260)

Dodelson S., 2004, PhRvD, 70, 023008

Ebeling H., Edge A. C., Bohringer H., Allen S. W., Crawford C. S., Fabian A. C., Voges W., Huchra J. P., 1998, MNRAS, 301, 881

Ebeling H., Edge A. C., Allen S. W., Crawford C. S., Fabian A. C., Huchra J. P., 2000, MNRAS, 318, 333

Eke V. R., Cole S., Frenk C. S., 1996, MNRAS, 282, 263

Evans A. K. D., Bridle S., 2009, ApJ, 695, 1446

Flores R. A., Allgood B., Kravtsov A. V., Primack J. R., Buote D. A., Bullock J. S., 2007, MNRAS, 377, 883

Gavazzi R., 2005, A&A, 443, 793

Hamana T., Miyazaki S., Kashikawa N., Ellis R. S., Massey R. J., Refregier A., Taylor J. E., 2009, PASJ, 61, 833

Hennawi J. F., Dalal N., Bode P., Ostriker J. P., 2007, ApJ, 654, 714

Henry J. P., 2000, ApJ, 534, 565

Henry J. P., Evrard A. E., Hoekstra H., Babul A., Mahdavi A., 2009, ApJ, 691, 1307

Ho S., Bahcall N., Bode P., 2006, ApJ, 647, 8

Ho S., Lin Y.-T., Spergel D., Hirata C. M., 2009, ApJ, 697, 1358

Hoekstra H., 2003, MNRAS, 339, 1155

Hoekstra H., Yee H. K. C., Gladders M. D., 2004, ApJ, 606, 67

Ilbert O., et al., 2009, ApJ, 690, 1236

Jee M. J., et al., 2007, ApJ, 661, 728

Jing Y. P., Suto Y., 2002, ApJ, 574, 538

Johnston D. E., et al., 2007, preprint (arXiv:0709.1159)

Kaiser N., Squires G., 1993, ApJ, 404, 441

Kaiser N., Squires G., Broadhurst T., 1995, ApJ, 449, 460

Kasliwal M. M., Massey R., Ellis R. S., Miyazaki S., Rhodes J., 2008, ApJ, 684, 34

Kasun S. F., Evrard A. E., 2005, ApJ, 629, 781

Katayama H., Hayashida K., Takahara F., Fujita Y., 2003, ApJ, 585, 687

Kawahara H., 2010, ApJ, submitted (arXiv:0911.0390)

Kazantzidis S., Kravtsov A. V., Zentner A. R., Allgood B., Nagai D., Moore B., 2004, ApJ, 611, L73

Keeton C. R., Kochanek C. S., Falco E. E., 1998, ApJ, 509, 561

Kitayama T., Suto Y., 1997, ApJ, 490, 557

Kneib J.-P., et al., 2003, ApJ, 598, 804

Koester B. P., et al., 2007, ApJ, 660, 239

Kolokotronis V., Basilakos S., Plionis M., Georgantopoulos I., 2001, MNRAS, 320, 49

Komatsu E., et al., 2009, ApJS, 180, 330

Koopmans L. V. E., Treu T., Bolton A. S., Burles S., Moustakas L. A., 2006, ApJ, 649, 599

Lee J., Suto Y., 2003, ApJ, 585, 151

Lin Y.-T., Mohr J. J., 2004, ApJ, 617, 879

Mahdavi A., Hoekstra H., Babul A., Balam D. D., Capak P. L., 2007, ApJ, 668, 806

Mahdavi A., Hoekstra H., Babul A., Henry J. P., 2008, MNRAS, 384, 1567

Mandelbaum R., Hirata C. M., Broderick T., Seljak U., Brinkmann J., 2006a, MNRAS, 370, 1008

Mandelbaum R., Seljak U., Cool R. J., Blanton M., Hirata C. M., Brinkmann J., 2006b, MNRAS, 372, 758

Mandelbaum R., Seljak U., Hirata C. M., 2008, JCAP, 8, 6

Mandelbaum R., Seljak U., Baldauf T., Smith R. E., 2010, MNRAS, submitted (arXiv:0911.4972)

Mantz A., Allen S. W., Ebeling H., Rapetti D., 2008, MNRAS, 387, 1179

McMillan S. L. W., Kowalski M. P., Ulmer M. P., 1989, ApJS, 70, 723

Medezinski E., et al., 2007, ApJ, 663, 717

Miralda-Escude J., 1995, ApJ, 438, 514

Miyazaki S., et al., 2002, PASJ, 54, 833

Mohr J. J., Evrard A. E., Fabricant D. G., Geller M. J., 1995, ApJ, 447, 8

Navarro J. F., Frenk C. S., White S. D. M., 1996, ApJ, 462, 563

Navarro J. F., Frenk C. S., White S. D. M., 1997, ApJ, 490, 493

Oguri M., Blandford R. D., 2009, MNRAS, 392, 930

Oguri M., Keeton C. R., 2004, ApJ, 610, 663

Oguri M., Lee J., Suto Y., 2003, ApJ, 599, 7

Oguri M., Takada M., Umetsu K., Broadhurst T., 2005, ApJ, 632, 841

Oguri M., et al., 2009, ApJ, 699, 1038

Okabe N., Umetsu K., 2008, PASJ, 60, 345

Okabe N., Takada M., Umetsu K., Futamase T., Smith G. P., 2010, PASJ, in press (arXiv:0903.1103)

Ostriker J. P., Steinhardt P., 2003, Sci, 300, 1909

Parker L. C., Hoekstra H., Hudson M. J., van Waerbeke L., Mellier Y., 2007, ApJ, 669, 21

Rhee G. F. R. N., van Haarlem M. P., Katgert P., 1991, A&AS, 91, 513

Richard J., et al., 2010, MNRAS, submitted (arXiv:0911.3302)

Rozo E., et al., 2010, arXiv:0902.3702

Sanderson A. J. R., Edge A. C., Smith G. P., 2009, MNRAS, 398, 1698

Schramm T., 1990, A&A, 231, 19

Sheldon E. S., et al., 2007a, preprint (arXiv:0709.1153)

Sheldon E. S., et al., 2007b, preprint (arXiv:0709.1162)

Sheth R. K., et al., 2003, ApJ, 594, 225

Smith R. E., Peacock J. A., et al., 2003, MNRAS, 341, 1311

Strazzullo V., Paolillo M., Longo G., Puddu E., Djorgovski S. G., De Carvalho R. R., Gal R. R., 2005, MNRAS, 359, 191

Tissera P. B., White S. D. M., Pedrosa S., Scannapieco C., 2010, MNRAS, submitted (arXiv:0911.2316)

Umetsu K., Broadhurst T., 2008, ApJ, 684, 177

Vikhlinin A., et al., 2009, ApJ, 692, 1060

Wang Y.-G., Fan Z.-H., 2004, ApJ, 617, 847

APPENDIX A: IMPACT OF A SUBPEAK ON CLUSTER SHAPE MEASUREMENTS

We conduct simple simulations to examine the impact of a single substructure on cluster shape measurements. We assume a main halo, modelled by an elliptical NFW profile, with $M_{\mathrm{main}} = 8 \times 10^{14} h^{-1} M_\odot$, $c_{\mathrm{vir}} = 6.0$, $e = 0.4$, $\theta_e = 0$ deg. We then add a spherical (i.e., $e = 0$) NFW subpeak, whose centre is chosen randomly, with its mass $M_{\mathrm{sub}} = f_{\mathrm{sub}} M_{\mathrm{main}}$. The concentration parameter of the subpeak taken to be same as that of the main halo. The cluster and source redshifts are assumed to $z_l = 0.3$ and $z_s = 1.0$, respectively. Given the mass model, we randomly distribute source galaxies in the $20' \times 20'$ region centred at the main halo with the number density of $n = 15$ arcmin^{-2}, and compute reduced shear for each galaxy. We then repeat the same fitting procedure used in this paper (§2), which assumes a single elliptical NFW component, to derive the shape and orientation of this compound system. All the source galaxies have the shape measurement uncertainty $\sigma_g = 0.4$. The effect of large-scale structure along the line-of-sight is not included in this simulation.

First we perform the simulation without any subpeak. We find that all the parameters are recovered well within 1σ statistical uncertainties, which validates our fitting procedure using two-dimensional square grids with a grid size of $1'$. The best-fit ellipticity and position angles are $e = 0.41^{+0.12}_{-0.25}$ and $\theta_e = -0.1^{+15.1}_{-19.0}$ deg, respectively.

Next we add a subpeak to see how the best-fit values can be biased. We consider three cases, $f_{\mathrm{sub}} = 0.1$, 0.2, and 0.4. For each case we generate 500 realisations with different subpeak locations. Figure A1 shows the result. We find that the effect of such a subpeak is modest. The subpeak can have significant (i.e., comparable to the statistical uncertainty) impact on cluster shape measurements only when
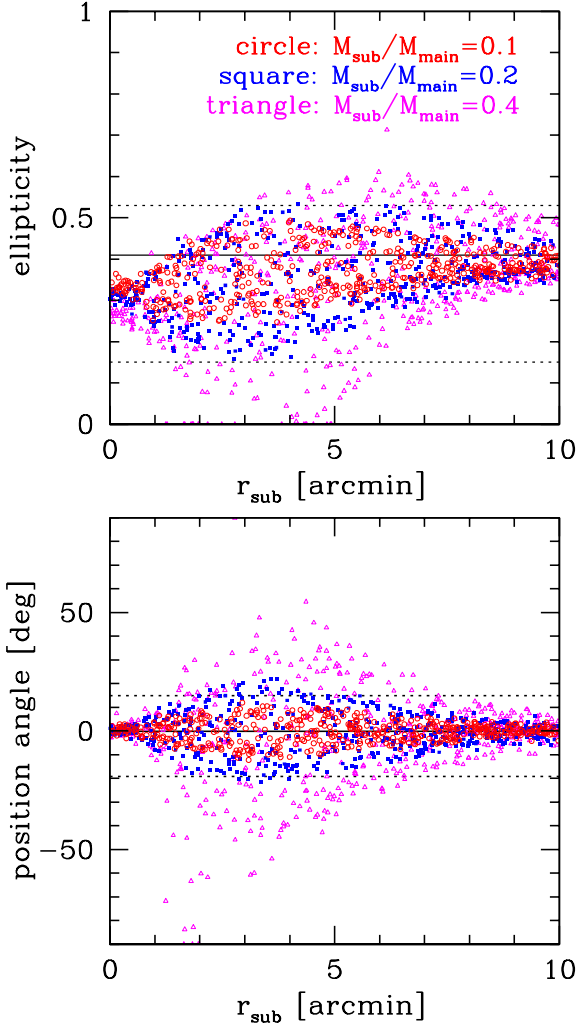
Figure A1. The effect of a subpeak on measurements of cluster ellipticities (*upper*) and position angles (*lower*). We consider three subpeaks with the mass ratio of $f_{\rm sub} = M_{\rm sub}/M_{\rm main} = 0.1$ (*squares*), 0.2 (*circles*), and 0.4 (*triangles*). We study the effect by placing a subpeak with its centre randomly chosen, fitting the two-peak system assuming a single elliptical NFW component, and deriving best-fit parameter values. We repeat this procedure 500 times for each mass ratio, and plot best-fit values as a function of the subpeak location from the main halo. Horizontal solid and dotted lines indicate best-fit values and marginalised 1σ errors in the absence of the subpeak. See text for more details.

$f_{\rm sub} > 0.2$, which appears to be quite extreme at least for the case that the subpeak is physically associated with the main halo. Interestingly, we find that the subpeak has the largest impact when it is located at $3' \lesssim r \lesssim 5'$ which is the most important region for constraining the cluster ellipticity (§4.1).

APPENDIX B: MASSES AND CONCENTRATION PARAMETERS FOR $\Delta = 500$

In this paper we have presented results for the virial overdensity $\Delta_{\rm vir}$. However, different values of the overdensity may be suited for various applications. For instance, X-ray ob-

Table B1. Best-fit masses and concentration parameters for the overdensity $\Delta = 500$.

Name	M_{500} $(10^{14}h^{-1}M_\odot)$	c_{500}
A68	$3.03^{+1.32}_{-0.71}$	$1.66^{+2.25}_{-1.24}$
A115	$5.19^{+0.36}_{-2.70}$	$0.48^{+0.01}_{-0.19}$
A209	$6.42^{+1.32}_{-1.48}$	$0.97^{+0.61}_{-0.32}$
RXJ0142	$2.75^{+0.61}_{-0.50}$	$2.73^{+1.94}_{-0.68}$
A267	$2.04^{+0.48}_{-0.35}$	$5.53^{+4.93}_{-1.89}$
A291	$2.70^{+0.88}_{-0.54}$	$1.30^{+1.40}_{-0.71}$
A383	$1.56^{+0.18}_{-0.13}$	$31.58^{+5.52}_{-4.68}$
A521	$3.79^{+1.32}_{-0.87}$	$0.53^{+0.37}_{-0.26}$
A586	$3.53^{+1.91}_{-0.90}$	$5.16^{+5.13}_{-2.72}$
ZwCl0740	$6.56^{+2.36}_{-2.64}$	$0.58^{+0.47}_{-0.23}$
ZwCl0823	$4.82^{+1.22}_{-1.44}$	$1.23^{+1.07}_{-0.60}$
A611	$4.46^{+1.10}_{-0.81}$	$0.69^{+0.76}_{-0.36}$
A689	$0.98^{+0.47}_{-0.54}$	$0.08^{+0.13}_{-0.03}$
A697	$6.79^{+1.32}_{-1.45}$	$0.90^{+0.63}_{-0.34}$
A750	$3.15^{+7.11}_{-1.24}$	$0.00^{+0.00}_{-0.00}$
A1835	$6.38^{+1.35}_{-1.41}$	$1.65^{+0.60}_{-0.47}$
ZwCl1454	$2.07^{+0.45}_{-0.80}$	$1.10^{+1.02}_{-0.76}$
ZwCl1459	$2.91^{+1.11}_{-0.64}$	$4.06^{+5.03}_{-1.68}$
A2219	$4.36^{+1.27}_{-0.81}$	$5.60^{+2.68}_{-2.74}$
RXJ1720	$2.26^{+0.92}_{-0.52}$	$6.32^{+7.62}_{-2.50}$
A2261	$5.74^{+1.40}_{-0.87}$	$2.86^{+0.95}_{-0.88}$
RXJ2129	$1.42^{+2.31}_{-0.56}$	$0.00^{+0.01}_{-0.00}$
A2390	$4.56^{+1.21}_{-0.85}$	$3.26^{+2.39}_{-1.22}$
A2485	$1.88^{+0.60}_{-0.55}$	$6.70^{+10.99}_{-4.10}$
A2631	$2.85^{+0.70}_{-0.60}$	$4.60^{+6.01}_{-1.77}$

servables are more directly connected with masses defined by the overdensity $\Delta = 500$ rather than the virial overdensity (e.g., Vikhlinin et al. 2009). Moreover, Okabe et al. (2010) showed that the fractional error on the cluster mass measured from weak lensing is also minimised for $\Delta \simeq 500$. In Table B1, we show our 2D shear fitting results adopting the overdensity $\Delta = 500$ instead of the fiducial virial overdensity $\Delta_{\rm vir} \simeq 110$. Note that constraints on the ellipticity, position angle, and the mass centroid are unaffected by the adopted value of Δ.